

AD-A250 960



①

**The Free Surface Signature of Unsteady,
Two-Dimensional Vortex Flows**

Dequan Yu and Grétar Tryggvason
Department of Mechanical Engineering and Applied Mechanics

Contract Number N0001-86-K-0684
Technical Report No. 89-03

April, 1989

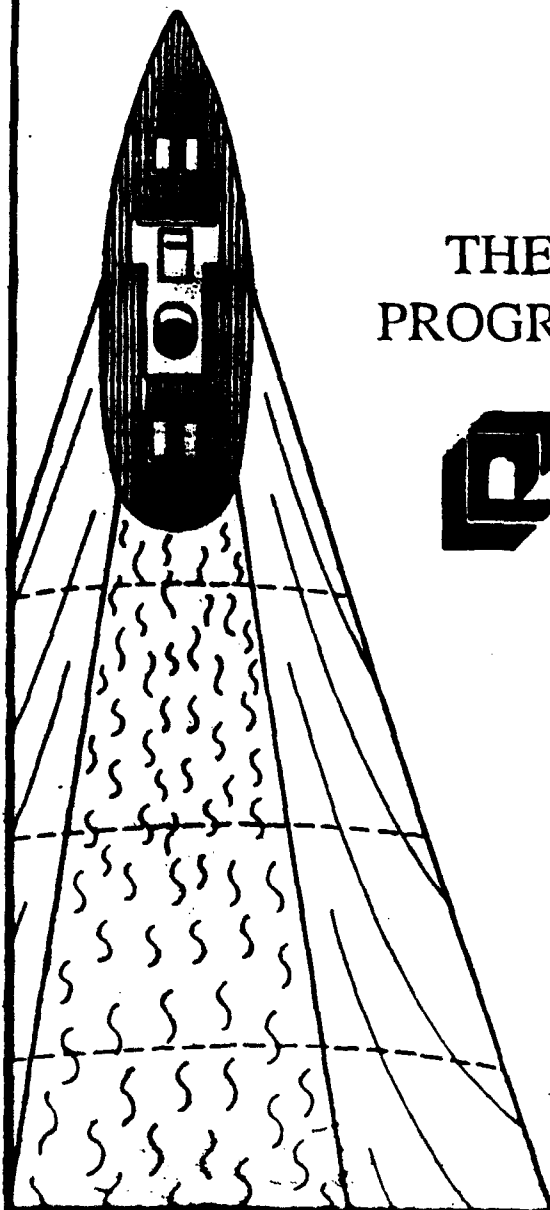
DISTRIBUTION STATEMENT A
Approved for public release;
Distribution Unlimited

DTIC
S **ELECTE** **D**
JUN 2 1992
C

92-13783



92 5 26 009



THE UNIVERSITY OF MICHIGAN PROGRAM IN SHIP HYDRODYNAMICS



COLLEGE OF ENGINEERING

**NAVAL ARCHITECTURE &
MARINE ENGINEERING**

AEROSPACE ENGINEERING

**MECHANICAL ENGINEERING &
APPLIED MECHANICS**

**SHIP HYDRODYNAMIC
LABORATORY**

**SPACE PHYSICS RESEARCH
LABORATORY**



**THE FREE SURFACE SIGNATURE OF UNSTEADY,
TWO-DIMENSIONAL VORTEX FLOWS**

Dequan Yu

Grétar Tryggvason

Department of Mechanical Engineering

and Applied Mechanics

The University of Michigan

Ann Arbor, MI 48109

Abstract. The interaction of two-dimensional vortex flows with a free surface is studied numerically using a combined vortex/boundary integral technique. The vorticity is modeled as point vortices, vortex sheets and finite area vortex regions. Two problems are studied in considerable detail, the large amplitude Kelvin-Helmholtz instability of a submerged shear-layer and the head-on collision of a vortex pair with the free surface. The surface deformation is controlled by a Froude number, based on the vortical motion, and the geometrical parameters describing the initial vortex configuration. Large Froude numbers generally lead to strong interactions for sufficiently shallow vortices.

Statement A per telecon Dr. Edwin Rood
ONR/Code 1132
Arlington, VA 22217-5000

NWW 6/1/92

Accession For	
NTIS GRA&I	<input checked="" type="checkbox"/>
DTIC TAB	<input type="checkbox"/>
Unannounced	<input type="checkbox"/>
Justification	
By _____	
Distribution/	
Availability Codes	
Dist	Avail and/or Special
A-1	



1. Introduction

The classical approximation in water wave theory is the assumption of irrotational fluid motion. This assumption not only makes the problem much more tractable but the results also account well for observations. While the motion of waves may generally be irrotational, any observer of river flow or ship wakes knows that vortical flow below the surface can generate considerable surface deformations. These surface motions have recently been the subject of several investigations. The motivation comes to a large extent from recent observations by remote sensing techniques, which have led to an interest in the wake of objects moving on a free surface. The most significant surface mark of a moving ship has been thought to be the wave pattern analyzed by Kelvin nearly a century ago. Observations by remote sensing devices have changed that perception. Often a narrow mark that persists for several hours is left by ships. The narrow angle rules out Kelvin wakes; although it is not completely clear whether subsurface motion or an alteration in the surface water composition leaves the detectable mark, the cause is likely to be the fluid motion in the wake. The wake consists of rotational, turbulent, high Reynolds number flow, and coherent motion could last for a very long time.

Sarpkaya (1986) studied the surface deformation due to the vortex system behind a lifting surface experimentally. He has identified two types of surface disturbances that he calls scars and striations. The scars are surface depressions that appear as a pair behind the body parallel to the direction of motion. These marks appear to be directly related to the trailing vortices and may be rather two-dimensional in a plane perpendicular to the motion (called the Trefftz plane by aerodynamicists). The striations, on the other hand, are perpendicular to the direction of motion and have a more three-dimensional character. Similar experiments have been performed by Willmarth and Hirska (1988), who also studied the surface deformation due to (essentially) two-dimensional vortex pairs. The two-dimensional vortex pair has also

been studied by Sarpkaya, Elnitsky II, and Leeker (1988). Earlier work on the collision of two-dimensional vortex pairs with a free surface was reported by Barker and Crow (1977), but in that work the main emphasis was on the vortex motion, rather than the surface deformations. Bernal and Madnia (1988) investigated the generation of surface waves due to a shear flow by considering a jet below a free surface, and Bernal and Kwon (1989) studied the interaction of a vortex ring with a free surface. The experimental observations suggest that many competing and interacting processes are responsible for the observed wave pattern. Not only are surface waves generated by the vortical flow, but the waves also radiate energy away from the disturbance region and thereby affect the flow itself.

Analytical investigations are, of course, limited to rather simple situations. Linearized solutions exist for a flow over a fixed vortex (e.g., Kochin, Kibel and Roze, (1964)) and for a vortex moving freely under a free surface (Wehausen and Laitone (1960)), while Novikov (1981) discusses the wave generation due to a periodic array of point vortices. For the full nonlinear solutions, however, it is necessary to turn to numerical techniques. Tryggvason (1988a) presents a brief numerical study of surface deformation due to roll-up of a submerged vortex sheet (a study extended in the present work), and the motion of a point vortex pair toward a free surface has been simulated by Sarpkaya, Elnitsky II, and Leeker (1988) and Telste (1989) using a generalized boundary integral/vortex method developed by Baker, Meiron and Orszag (1982). Marcus (1988) simulated the same problem by a finite difference technique.

The generation of wake vorticity by ships is reasonably well understood. Saunders (1965) discusses the overall character of the vortices sheet by a ship, and Lugt (1981), in his excellent survey of vortex motion in ship hydrodynamics (as well as in his more general exposure of vortex motion, Lugt (1983)), gives several examples.

Considerable progress has been made in numerical simulations of the nonlinear evolution of large-amplitude surface waves during the last decade. Among of the

first calculations of large-amplitude surface waves by boundary integral methods is Longuet-Higgins and Cokelet's (1976) calculations of the large-amplitude motion of a breaking wave. These methods have now reached sufficient maturity that simulations of two-dimensional large-amplitude surface waves are relatively routine, see, for example, Vinje and Brevig (1981), Dold and Peregrine (1986), and Schultz (1987). A general method for flows with arbitrary stratification and an efficient iterative solution technique are presented by Baker, Meiron and Orszag (1982). For a general review of vortex methods for two-dimensional flows, see Leonard (1980) and Sarpkaya (1989).

In this paper, we study the generation of surface disturbances by a submerged vortical flow and the effect of the free surface on the evolution of vortical flow. The flow is assumed to be inviscid, incompressible, and two-dimensional, and a combined vortex/boundary integral technique is used. The vorticity is modeled as point vortices, vortex sheets, and finite area vortex regions. Two problems are studied in considerable detail: the large-amplitude Kelvin-Helmholtz instability of a submerged shear-layer and the head-on collision of a vortex pair with the free surface. The evolution is controlled by a Froude number, based on the vortical motion, and the geometrical parameters describing the initial vortex configuration. We deal exclusively with free surface problems, but several of the same phenomena may be observed if the free surface is replaced by a density interface. For a study of one such problem, see Dahm, Scheil, and Tryggvason (1989).

The rest of the paper is arranged as follows: Section 2 discusses the mathematical model, the numerical method, and the relevant dimensionless parameters. The method is a straightforward extension of the method described by Baker, Meiron and Orszag (1982); hence, we only give a brief description. In Section 3 we present our results, first for the large-amplitude Kelvin-Helmholtz instability of a shear layer, then for the head-on collision of a vortex pair with the free surface. We show representative

time evolution and discuss the accuracy and the effect of the numerical parameters. The large-amplitude stage for several values of the control parameters is shown, and various diagnostic quantities are discussed. Our conclusions and discussions of future work appear in Section 4. A short account of some of the work reported here was presented at the American Physical Society, Division of Fluid Dynamics, annual meeting at SUNY, Buffalo (Song, Yu and Tryggvason (1988)). A brief discussion of preliminary results can be found in Tryggvason (1988a, 1988b) and Willmarth et al. (1989).

2. Problem Formulation and Numerical Method

The formulation of inviscid, free-surface problems in terms of generalized vortex sheets is well known, so only a brief discussion will be given here. For a fairly complete discussion and the original developments, the reader is referred to Baker, Meiron, and Orszag (1982).

In all our calculations we assume periodic horizontal boundary conditions. The velocity of a (generalized) vortex sheet of strength γ can then be calculated by

$$q^*(s) = u - iv = \frac{1}{2i} \int_0^1 \gamma(s') \cot \pi(z(s') - z(s)) ds' + q_{ext}^* \quad (2.1)$$

where the integral is over both the free surface and the vortex sheet, and q_{ext}^* is the velocity due to boundary conditions, or vorticity not confined to a vortex sheet. We generally follow Baker, Meiron, and Orszag's work (1982) and integrate the dipole sheet strength, $\mu = \phi_1 - \phi_2$ (ϕ is velocity potential), in time and find $\gamma = \partial\mu/\partial s$. The evolution equation for μ is found by subtracting the Bernoulli equation on each side of the sheet, yielding

$$\frac{D\mu}{Dt} = A \left(2 \frac{D\Phi}{Dt} - \bar{U} \cdot \bar{U} + \frac{1}{4} \gamma^2 + 2gy + \frac{\sigma}{\rho_2 - \rho_1} \kappa \right) \quad (2.2)$$

A is the Atwood ratio $A = (\rho_1 - \rho_2)/(\rho_2 + \rho_1)$ and Φ is the average of the velocity potential on either side of the integral. To find $d\Phi/dt$, we take the Lagrangian time derivative of the real part of Cauchy's integral formula for a periodic domain

$$W(z) = \Phi + i\Psi = \frac{1}{2i} \int_0^1 \mu(s') \cot \pi(z' - z) dz' \quad (2.3)$$

and substitute the result into (2.2) to obtain an integro-differential equation for the evolution of μ .

To extract the appropriate nondimensional groups, we cast the above equations into nondimensional form. We construct our time scale from the characteristic length of the rotational flow, L , and the characteristic velocity, Γ/L , where Γ is a circulation

describing the total strength of the vorticity field. A time scale is then given by L^2/Γ .

With the nondimensional variables defined as

$$(x, y) = L (\tilde{x}, \tilde{y}), \quad t = L^2/\Gamma \tilde{t}, \quad (\bar{U}, \gamma) = \Gamma/L (\tilde{U}, \tilde{\gamma}), \quad (\Phi, \mu) = \Gamma (\tilde{\Phi}, \tilde{\mu}) \quad (2.4)$$

the nondimensional form of the equation for the vortex sheet strength becomes (dropping the tilde)

$$\frac{D\mu}{Dt} = A \left(2 \frac{D\Phi}{Dt} - \bar{U} \cdot \bar{U} + \frac{1}{4} \gamma^2 + 2 \frac{1}{Fr^2} y + \frac{1}{We} \kappa \right) \quad (2.5)$$

where $Fr = \sqrt{\Gamma^2/gL^3}$ is a Froude number, and $We = \Delta\rho\Gamma^2/\sigma L$ is a Weber number.

The nondimensional groups specifying our problem are therefore the Froude number, Fr , the Weber number, We , and the geometric parameters describing the initial condition. The Atwood number, A , is always equal to unity for the free-surface case studied here, and in most of our calculations we assume infinite Weber number. This scaling essentially ignores the presence of the free surface, and same nondimensional time therefore means that the vortex sheet roll-up has progressed equally far, independent of the Fr . Obviously, this is not the only possible scaling. We could also base our nondimensionalization solely on the free surface, in which the basic nondimensional parameter would be a nondimensional vortex strength equivalent to the Froude number. The time scale would be different though. We feel that the current "vortex scaling" is the reasonable one, since the vortical flow is what drives the motion. We should note that in Tryggvason (1988a, 1988b), as well as in Dahm et al. (1988), the basic nondimensional parameter is written as $R = gL^3/\Gamma^2 = 1/Fr^2$. Clearly there is a one-to-one correspondance with the current notation.

Notice the appearance of the vortex strength in the Weber number. Intense vortices (large Γ , small L) can interact with the surface in a gravity-dominated way, even if surface tension is large, and waves of length L would be capillary waves in the absence of vorticity.

The assumption of periodic boundary conditions is the usual one for shear layer simulations in which many similar vortical structures are evolving in essentially the same way; but for the collision of a vortex pair with the surface, an infinite domain would be more natural since single pairs are usually generated experimentally. In the case of the vortex pair, we have checked the effect of the period length and found that the results are only minimally affected by changes in the length (compared with the separation of the vortex pair) once a minimum length is achieved.

In those calculations where the vorticity is modeled as vortex sheets we use a vortex blob to prevent the vortex sheet from forming a singularity and to reduce the growth of short-wave instability. Krasny (1986) shows that in contrast to simulations that do not employ any regularization, vortex blob methods, for any finite blob size, produce smooth and well behaved solution, for sufficiently accurate calculations. The evolution in the vortex center will depend on the blob size, but the effect on the large-scale structure is minimal. (This will be demonstrated when we present our results.) For further discussions of the vortex blob regularization, the reader is referred to Krasny (1986, 1988) and Tryggvason (1989).

Occasionally, a saw-tooth instability on the free surface appears in our computations. This instability is common in boundary integral calculations, and can generally be controlled by slight smoothing, see Longuet-Higgins and Cokelet (1976). The numerical filtering is employed rarely at the beginning of the calculation and more frequently later. We have found that the dipole formulation, described above, is more robust than the vorticity formulation, which was used for the calculations in Tryggvason (1988a, 1988b). The calculations generally had to be terminated when the free surface formed a sharp corner and difficulties in obtaining rapid convergence were experienced. Although we expect such regions of high curvature to indicate a breakdown of our model (small-scale phenomena such as viscosity and surface tension have been ignored) there is not direct relation to loss of convergence and, say,

wave breaking. For example, simulations of the Rayleigh-Taylor instability encounter the same difficulty under somewhat different conditions. We generally terminate our calculations when the number of iterations required for convergence is about ten or fifteen. Occasional redistribution of the free-surface points was used in some of our runs. The time integration was done by STEP from Champine and Gordon (1965).

In some of our calculations we take the vorticity to be patches, or strips, of uniform vorticity, called Finite Area Vortex Regions (FAVR's) by Zabusky, Hughes and Roberts (1979). Because of some mathematical difficulties in calculating $D\Phi/Dt$ in eq. (2.3), we integrate the vortex sheet strength directly, as done by Tryggvason (1988a), instead of using the dipole strength as in the other calculations presented here. The evolution equation for the vortex sheet strength of the free surface is obtained either by differentiation of eq. (2.5) or by subtracting the tangential component of the Euler equations on either side of the interface. This equation contains dU/dt , which is given by the Lagrangian time derivative of the Biot-Savart law and the velocity contribution from the FAVR's:

$$q_{ext} = u + iv = \frac{\omega}{2\pi} \oint_c (\log |\sin \pi(z - z')|) dz' \quad (2.6)$$

the integral is over the boundary of the region containing uniform vorticity.

3. Results and Discussion

We have studied the surface deformation due to both the large-amplitude roll-up of a shear layer below a free surface and the collision of a vortex pair with a free surface. In both cases we have modeled the vortical flow in three ways, as point vortices, vortex sheets, and finite area regions of uniform vorticity (vortex patches). The results for the shear layer are presented in Section 3.1, and Section 3.2 contains the vortex pair study.

3.1 Shear Layer Under a Free Surface

We consider a periodic free surface with flow parallel to the surface. At depth d there is a shear layer such that the velocity changes abruptly. Our frame of reference moves with the average of the velocity above and below the shear layer, so that a vortex generated by a large-amplitude Kelvin-Helmholtz instability would be stationary if the free surface was absent. The period length, L , is taken as a length scale, and the evolution is governed by the Froude number, the relative depth of the shear layer, d/L , and, possibly, the internal structure of the layer.

We first model the shear layer as a vortex sheet across which there is a discontinuous change in tangential velocity. To regularize the vortex sheet and prevent both the growth of a short-wave Kelvin-Helmholtz instability and the formation of a singularity, we use vortex blobs to represent the sheet. We use the algebraic blob employed by Krasny (1986) with blob size, $\delta = 0.1$. Several of our vortex sheet runs have been repeated with different blob radii to check that the effect of finite δ is minimal and confined to the vortex cores.

Figure 1 shows the evolution of a vortex sheet perturbed by a single wave below a free surface; $Fr = 0.5$ and $d/L = 0.2$. The free surface is represented by 200 computational elements, and the vortex sheet by 200 vortex blobs. The free surface is initially flat, but the vortex sheet is given a slight perturbation. As the vortex sheet rolls up, the induced velocity causes a depression in the free surface that remains

relatively stationary slightly to the front (or left) of the vortex. As the amplitude grows, the trough becomes steeper on its left side and eventually turns over.

To verify this run, it was repeated with different numbers of computational elements and different size of vortex blobs. A comparison between three different runs at a late time is shown in figure 2. The nondimensional time is 1.25; figure 2a is the last frame from figure 1, 2b is with same resolution but $\delta = 0.2$, and in 2c $\delta = 0.2$, and 50 points are used to represent the free surface, and 50 blobs for the vortex sheet. Except for a small difference in the region of highest curvature and in the core of the vortex, the results are virtually identical.

Figure 3 shows the large-amplitude stages for several values of Fr and d/L . The columns correspond to different relative depth (0.2, 0.3, and 0.4), and the rows to different Froude number (1.0, 0.5, 0.354, and 0.25). The nondimensional time for the first column is 1.25, for the next one, 1.6, and for the last one, 2.0. At these times, generally one run in the column encounters numerical problems. Since the amplitude of the free surface motion is too small to show up clearly in some of the frames in figure 3, we show several of the free surface profiles amplified five or ten times in figure 4 (the letters correspond to those in figure 3). Many of these runs have been checked by grid refinement and smaller δ , and are generally found to be insensitive to the numerical resolution and blob size. As the parameters change there are clearly identifiable trends. For fixed d/L , the overall amplitude increases with increasing Fr , and for fixed Fr , the amplitude decreases with increasing d/L . Hence, a strong, shallow sheet (figure 3a) deforms the surface most while a deep, weak vortex sheet (figure 3l) has the least effect. We can identify a least three scenarios for the large-amplitude evolution. For the strong, shallow vortex sheet, figure 3a, the vortex pulls the interface down and will eventually entrain the top fluid (air). For weaker, deeper sheets, figure 3b to f, the free surface develops into a breaking wave whose character depends on the parameters. (The wave in figure 3d is reminiscent of a plunging breaker, but in

figure 3h would be classified as a spilling breaker.) For the weakest, deepest waves, the long initial wave degenerates into several smaller waves. Other examples showing these different flow regimes are discussed briefly by Tryggvason (1988a).

To quantify the evolution of the free surface in the runs in figure 3, we have plotted a few parameters in figure 5 that might characterize the evolution. For clarity, the figure is divided into three columns, according to the value of d/L : (i) is for $d/L = 0.2$, (ii) for $d/L = 0.3$ and (iii) for $d/L = 0.4$. The letter identifying each line corresponds to figure 3. The overall amplitude (from crest to trough) is plotted versus time in (a). As stated before, the amplitude depends strongly on both Fr and d/L , and figure 5a reflects this clearly: in each frame the growth rate decreases with decreasing Froude number, and comparisons between the different frames show that the growth rate decreases with d/L .

In figure 5b, the horizontal location of the minimum point (the maximum depression) is plotted versus time. Initially, when the amplitude is still infinitesimal, the depression is slightly to the left of the vortex for all cases. For high Froude number this depression moves further to the left, but for lower Froude numbers it moves to the right, closer to the vortex. For shallow vortices, this motion eventually reverses and the depression moves away from the vortex again, but for deeper vortices the depression seems to stabilize close to the vortex (right above the vortex in the case of the lowest Froude number). Notice that for a fixed time there is much greater difference in the location of the depression for the deep vortices than for the shallow ones. In some sense, the shallow vortices appear to attract the depression to a fixed location independent of the Froude number. The slight oscillations for low Froude number and deep vortex sheets are indicative of the generation of shorter, smaller waves.

We have also expressed the free surface as

$$y(x) = \sum_{n=1}^{\infty} a_n \cos(2\pi nx - \theta_n)$$

and in figure 5c the amplitude, a_n , and in figure 5d the phase, θ_n , of the first mode are shown versus time. Since some of the waves have broken and the y-coordinate is a double-valued function of x, the final part of some of the curves may give modest insight. The information in these figures closely relates to those in figures 5a and b: the amplitude decreases with increased depth and decreasing Froude number, and the phase change depends on the parameters in similar way as the position of the depression. Notice, in particular, that the initial development of the phase angle (up to about nondimensional time 0.7) does not depend on d/L at all, even though the amplitude does. The same independancy is also observed in the position of the maximum depression, figure 5b. We have investigated the higher modes, but we generally find them less informative.

In the cases considered here, the free surface has only a minor effect on the evolution of the vortex sheet. Figure 6 illustrates the difference between the extreme cases, run (a) and run (l) from figure 3. Figure 6a shows the position of the vortex center, including both the x and the y coordinate. For run (l) the vortex center does not move at all, but in run (a) the vortex center moves slightly down and to the right. While the surface deformation in (a) is quite substantial, the differences are relatively minor. Figure 6b compares the evolution of the second moments, and again, for the time shown here, the difference is quite small. All other cases fall between these two.

Although the effect of the vortex blob size was minimal in most cases so far, the solution with a finite blob size is not exactly a solution to the Euler equation; furthermore, there is no direct relation between the size of the blob and a physical stabilization mechanism such as a finite thickness. To investigate the effect of finite thickness we have repeated several of the simulations in figure 3 using a layer of uniform vorticity, i.e., finite area vortex regions, (FAVR) to model the shear layer.

(For a study of roll-up of a layer of uniform vorticity in the absence of a free surface see e.g. Pozrikidis and Higdon (1985).)

Figure 7 shows the roll-up of the finite thickness vortex sheet for $d/L = 0.2$ and $Fr = 1$. The depth, d , is taken to the centerline of the vortex layer, and the thickness of the layer, t , is 0.1 times the length of the period, or $t/L = 0.1$. While the evolution is similar to the corresponding vortex sheet run (figure 3a), the deformation rate is smaller for the finite layer. In figure 7b, the solution is shown at time 2.4 for the same Froude number and depth, but $t/L = 0.15$. We note that finite thickness vorticity layers have a most unstable wavelength (at $t/L \approx 0.127$) as opposed to vortex sheets, which are more unstable at shorter disturbance lengths. Since the thickness in our simulations is close to this value, the slower growth of the disturbances in figure 7 is presumably a more realistic prediction for a real shear layer. The solution at a relatively long time is shown for $Fr = 0.5$ and $d/L = 0.2$ in figure 8 and for $Fr = 0.354$ and $d/L = 0.3$ in figure 9. In figure 8a, $t/L = 0.1$ and time = 1.75; in 8b, $t/L = 0.15$ and time = 2.4; in 9a, $t/L = 0.1$ and time = 2.1; and in 9b, $t/L = 0.15$ and time = 3.0. In both cases the same behavior as was seen in figure 7 is observed: the finite thickness slows down the evolution.

In figure 10 the amplitude and phase of the first mode are compared with the vortex sheet runs in figure 3; (a) depicts the runs in figures 7 and 3a, (b) the runs in figures 8 and 3e, and (c) the runs in figures 9 and 3i. The amplitude growth obviously depends on the thickness, with the thinner layer in reasonable agreement with the vortex sheet calculations for the lower Froude numbers. The phase, however, depends much less on the thickness and differs from the vortex sheet calculations in all cases. The basic conclusion from this figure is that we may expect the free surface signature to show some dependency on the internal structure of the shear layer.

During the initial stage in all cases and for a long time when the vortex sheet is deep and weak, the surface deformation is quite small. It is therefore natural to

ask whether linear analysis is applicable under these circumstances. Unfortunately, it is not. The vortex sheet propagates far into the nonlinear region, and analysis for the linear stage of the roll-up would cover only a very short time interval with respect to the surface evolution. We therefore propose a model based on the well-known observation that roll-up is initially associated with the strong advection of vorticity toward the vortex center, but once the vortex forms, it undergoes only moderate changes. Our model simply assumes that the roll-up process corresponds to an instantaneous creation of a point vortex. This, of course, is not completely correct. Apart from the fact that the vortex forms in a finite time, not all the vorticity ends up in the vortex. Therefore, the evolution should be faster according to this model, and the best agreement might be between the model and the full simulations when the point vortex contains only a part of the vortex sheet circulation.

Results from the numerical calculation with $Fr = 1.0$ and $d/L = 0.2$ are shown in figure 11. This selection of parameters corresponds to figure 3a. The free surface and the position of the single point vortex are shown. The circulation of the point vortex is relatively strong, and the free surface is pulled into the fluid. The evolution is similar to figure 3a, but faster, as expected, since the circulation is immediately confined to the point vortex. In figure 12, $Fr = 0.5$ and $d/L = 0.3$. Here the surface wave becomes increasingly steeper, eventually forming a sharp corner, which suggests a breaking wave as in figure 3e. Again, the evolution is much faster than the vortex sheet model. In figure 13, we show the evolution of the free surface (amplified 200 times) for a very low Froude number and shallow vortex ($Fr = 10^{-4}$ $d/L = 0.05$). To resolve the short waves that appear, we use 200 points on the free surface. As the vortex is started impulsively, a wave appears on the free surface and propagates away from the vortex. New waves are continually generated by the vortex, but the amplitude decreases.

We do not present a detailed comparison of any of the quantitative measures for

these flows and the previous simulations. It is sufficient to say that although the main characteristics are captured by the point model (e.g., we observe entrainment, breaking waves and short wave generation), the quantitative agreement is considerably worse than between the two other models. As we pointed out already, this is to be expected: the vortex is neither created instantaneously nor does it contain all the initial circulation.

We will, however, use the point vortex model for another purpose. When a vortex is relatively weak (that is, Froude number is low) the free surface motion is very small, and our fully nonlinear solution should compare well with a linearized solution. The linearized solution for the problem at hand is given by Wehausen and Laitone (1960) as linear nondimensional variables,

$$W(z, t) = \frac{1}{2\pi i} \ln\{(z-c)(z-\bar{c})\} + \frac{1}{\text{Fr}} \frac{1}{\pi i} \int_0^t d\tau \int_0^\infty \frac{e^{-ik\{z-\bar{z}(\tau)\}}}{\sqrt{k}} \sin\left\{\sqrt{\frac{k}{\text{Fr}}}(t-\tau)\right\} dk \quad (3.1)$$

where $W(z, t)$ is the complex velocity potential; z is the complex variable $x + iy$; and $c(t)$ is the location of the point vortex ($a + ib$). The bar on c denotes a complex conjugate. The velocity of the point vortex is

$$\dot{a}(t) - i\dot{b}(t) = -\frac{1}{4\pi b(t)} - \frac{1}{\text{Fr}} \frac{1}{\pi} \int_0^t d\tau \int_0^\infty \sqrt{k} e^{-ik\{c(t)-\bar{z}(\tau)\}} \sin\left\{\sqrt{\frac{k}{\text{Fr}}}(t-\tau)\right\} dk \quad (3.2)$$

and the surface elevation is

$$\eta(x, t) = -\frac{1}{\pi} \text{Im}\left\{\int_0^t d\tau \int_0^\infty e^{-ik\{x-\bar{z}(\tau)\}} \cos\left\{\sqrt{\frac{k}{\text{Fr}}}(t-\tau)\right\} dk\right\} \quad (3.3)$$

Numerical evaluation of equations (3.2) and (3.3) has been done by Hong (1987), who also approximated the equation for the wave elevation for small time as

$$\eta(x, t) = \frac{t}{2\pi} \left\{ \frac{x-a(t)}{b_0^2 + (x-a(t))^2} + \frac{x-a(0)}{b_0^2 + (x-a(0))^2} \right\} \quad (3.4)$$

The linearized solution above is for an infinite domain, while our calculations are for a periodic domain. However, if the depth of the point vortex is very small compared to the length of the domain, the effect of the finite period length is negligible. A

comparison of the small-time solution (equation (3.4)) with our calculation is shown in figure 14 (a) and (b). The parameters are $Fr = 1.22 \times 10^{-9}$, $d/L = 0.005$, and we have used 600 points to represent the surface (This large number is necessary since the vortex is very shallow, and the depth d sets the resolution requirement.). In figure 14a, the nondimensional time is equal to 0.0485, while in the figure 14b the nondimensional time is equal to 0.095. At the earlier time there is almost perfect agreement, but at the later time a slight deviation is observed. For a later time, it is necessary to use the full linear solution (not the short time expression), and a comparison of our calculation with equation 3.3 is given in figure 14c. The time is 0.42, and calculations for both 300 and 600 points are shown. Obviously, the overall agreement is good, but the 600-point calculation is slightly closer to the linearized solution.

The inviscid models studied here are all scale invariant and, thus, applicable to a wide range of physical length scales. In a ship's wake, for example, we would generally expect that while the results for small Froude number might describe the largest scales of the flow, the high Froude number results, where the vortical flow leads to rather dramatic "splashes", would be more applicable to the small-scale turbulent motion (such as the generation of "white water wakes" due to propellers). At small scales, however, the scale invariance of the inviscid model is broken by either viscosity or surface tension. While viscosity is not easily incorporated into our model, surface tension is.

We have looked at how surface tension modifies our solution, but before we present the full vortex/free surface case, in figure 15 we check how well our method follows the propagation of a linear capillary wave (For a discussion of surface tension effects on steep waves see, e.g., Hogan (1981). For implementation of surface tension in a boundary integral methods see, for example, Pullin (1982).). In the linearized

solutions the free surface amplitude is (e.g. Lamb (1932))

$$\eta = a \sin(kx + \sigma t) \quad (3.5)$$

and the dipole sheet strength is given by

$$\mu = -2 \frac{\sigma a}{k} \cos(kx + \sigma t) \quad (3.6)$$

where

$$\sigma^2 = gk + \frac{T}{\rho} k^3 \quad (3.7)$$

so the wave speed is

$$c^2 = \frac{g}{k} + \frac{T}{\rho} k \quad (3.8)$$

a is the initial (infinitesimal) amplitude, and k is the wave number. In figure 15a, the computed speed is compared with the theoretical speed for several values of surface tension. Here, λ is the wavelength, and λ_m is the wavelength with smallest speed, $\lambda_m = (2\pi/k_m) = 2\pi(T/\rho g)^{1/2}$; our results are for $\lambda/\lambda_m = 0.151, 0.302, 1.004, 1.92,$ and 3.33 . In figure 15b, we show the free surface elevation after the wave has propagated one-half wavelength for $\lambda/\lambda_m = 0.302$: (i) is the initial profile at time zero, (ii) is the computed profile, and (iii) is the theoretical prediction. Obviously, our numerical calculations (with 200 points per wavelength to resolve the free surface) compare rather well with the linear solution.

The effect of surface tension on the free surface deformations due to a vortex sheet roll-up is shown in figure 16; $Fr = 1$, and $d/L = 0.2$ corresponding to figure 3a. The solid line indicates $We = 0.33$, the long dashed line is for $We = 1.0$, and the dashed line is the infinite Weber number solution from figure 3a. The major effect of surface tension is to reduce the surface deformation in regions of highest curvature.

We end this section with a simulation of a more complicated situation: the pairing of roll-up vortices under a free surface. In figure 17, $Fr = 1.0$, and $d/L = 0.3$, the same as in figure 3c. The regularization parameter, however, has been taken somewhat

larger ($\delta = 0.2$) to limit the number of computational elements needed to represent the inner part of the roll-up vortices. The vortex sheet is initially perturbed by two sine waves, one with a wavelength equal to the period length, and the other half as long and with three times the amplitude of the longer wave. First, the vortex sheet rolls up into two distinct vortices, and the surface deformation is similar to what is predicted for a single wave in half the domain ($Fr = \sqrt{2}$ and $d/L = 0.3$). Then the vortices pair and drastically change the surface signature. We have run a few similar cases and generally found that (a) for shallow vortices the pairing process quickly leads to high curvature that inhibits further simulations, and (b) for deeper vortices the surface deformation is generally dominated by the pairing process.

3.2 Vortex Pair Approaching a Free Surface

Here we discuss the head-on collision of a vortex pair with a free surface. The surface is initially flat, and we use periodic boundary conditions in the horizontal direction. The evolution is somewhat dependent on the length of the period and slightly different from what would be observed in an infinite domain. However, our domain is generally sufficiently large so that the overall scenario is not altered. The initial vortex separation is taken as a length scale in the definition of the Froude number and the Weber number is infinite, unless otherwise noted.

Figures 18 to 20 show the collision for three different Froude numbers (11.2, 3.54, 1.58, respectively). The initial depth of the pair is 1.25 times the vortex separation, and the period length is five times the separation. In figure 18, a rather severe surface deformation occurs: as the vortex pair approaches the surface, it pushes the surface upward; and subsequently the pair propagates out of the main fluid region, carrying a considerable amount of fluid (a "blob") with it. At the same time, since the period length is relatively small compared to the vortex separation, the level of the fluid left behind drops to conserve mass. The speed of the vortex pair is only minimally affected by the presence of the free surface. Baroclinically generated vorticity at the

free surface obviously opposes the point motion, but at the same time pushes them slightly together, compensating for the effect of the surface. Shortly after the last stage shown, the iterative procedure failed to converge, and the calculations were terminated. Notice that the fluid in the "blob" remains almost constant at least for the duration of this simulation (this is easily seen by plotting the profiles on the same graph). Figure 19 shows the evolution for a smaller Froude number, 3.54. The initial surface deformation is similar to the high Froude number case, but after the initial bump forms, the vortices start to move apart and the rise of the fluid stops. At the same time, the interface is rapidly pulled down outward of the vortices, leading to entrainment of the top (zero density) fluid. For $Fr = 1.58$, in figure 20, the surface deformation is reduced, and the vortices move outward much like the surface was a solid wall. A small depression forms outward of the vortices eventually turning over into a breaking wave.

Several runs with other values of the Froude number confirm that the motion can be classified two ways: the large Froude number case, where the vortices propagate through the free surface, as in figure 18, and the small Froude number case where the free surface acts as a rigid boundary, as in figure 20. The transition from one type of motion to another takes place over a relatively small range of Froude numbers, and once these limits are reached the motion is relatively weakly dependent on the actual value of the Froude number.

In figure 21 we have plotted the solution at long time for several "high" Froude numbers and several "low" Froude numbers. Frames a, b, c are at time 10, for Froude numbers 11.2 (figure 18), 15.8 and 22.4. It is obvious that doubling the Froude number has rather minor effects. Frames d, e, f are for Froude numbers 0.5, 0.79, 1.58 at time 9.0. Although the overall shape of the surface deformation is similar, some changes occur as the Froude number decreases, in addition to the amplitude. A closer inspection (substantiated by additional runs) shows that the position of the

maximum surface depression is closer to the vortex for the lower Froude number, so that in the limit of zero Froude number we would expect the depression to coincide with the vortex position. This is in agreement with what we observed in the previous section and with Novikov's (1981) analytical, small-amplitude prediction for a vortex moving steadily below a free surface.

To quantify our results, we plot some quantitative information versus time in figures 22 and 23 for the three runs in figure 18 to 20. The maximum and minimum surface elevation is shown in figure 22a. The maximum surface elevation for the largest Froude number increases continuously, while for the intermediate case, the upward motion stops. For the lowest Froude number the elevation reaches a maximum at a much lower level than in the other runs and changes only slightly during the last part of the run. Initially, the minimum elevation is also the greatest for the high Froude number case; at the later time, however, the surface in the other two cases continues to be pulled down, while the high Froude number case levels off.

A plot of potential energy versus time, in figure 22b, reflects the amplitude of the surface motion seen in figures 18 to 20, and 22a. For the large Froude number case, the potential energy increases continuously, reaching an approximately constant growth rate at the end of the run. At the end of the run for the intermediate Froude number, the potential energy levels off and may decrease, and in the small Froude number case, the growth is oscillatory and considerably smaller. (Notice that the scale is different for the graphs.) The oscillations in the low Froude number case are presumably partly due to transients set up by the impulsive generation of the point vortices.

To show the effect of the surface on the vortical motion we plot the path of the vortices in figure 23 for the runs in figures 18 to 20. Dots on the path at regular time intervals, equal to 1.0, to give an indication of the speed. In the large Froude number case, where the vortices penetrate the interface, the paths converge, and the

reduction in distance between them more than compensates for the reaction from the surface, so that their speed increases. The vortices in the weak case move outward as if the surface was a solid wall. However, their path differs slightly from the solid wall case, due to the surface deformations and a small rebounding is seen. The intermediate path first diverges slightly and then turns inward. These calculations could not be continued past the point shown, but we expect that the vortex would eventually complete a loop and move outward. Such behavior is observed for vortices encountering weak density interfaces, see Dahm et al. (1989).

To address the influence of the relatively short period length used in our calculations, we have repeated some of them for a different size domain. In figure 24, the large-amplitude stage of three runs with the same Froude number (as in figure 18) and nondimensional time, 9.3, but with different period lengths are plotted. The main effect is that the fluid level below the blob vortex is lower for smaller periods, and the vortex pair moves slightly slower in shorter boxes due to the influence of the vortices in the neighboring periods. In the absence of a free surface the velocity of the vortex pair in (a), (b), and (c) would be 0.685, 0.865, and 0.925, respectively, times the velocity in an infinite domain. The relatively weak influence of the boundaries is therefore somewhat unanticipated, but apparently the greater increase in potential energy for the short period case compensates partly for the influence of the neighbors. For blobs of equal size, this lowering is larger, the shorter the period. In addition to the length of the periodic box, we have also run several cases with different initial vortex depth and found only minimal effects.

We have repeated some of our calculations with a higher number of computational elements and monitored the energy balance to assess the accuracy of our methods. For the range of computational elements used here, doubling the number of elements had virtually no effect. The accuracy of our calculations is also reflected by the almost total conservation of energy, which is generally a rather sensitive measure of a solu-

tion's quality. In figure 25, the potential energy, the finite part of the kinetic energy, and the total energy are plotted versus time for the run in figure 18. Obviously, even for the relatively modest number of points used (200), the energy is nearly completely conserved. We have found this to be generally true; only at the end of our calculations, where the solution procedure fails to converge, does the energy conservation deteriorate. Calculations similar to those discussed here have been reported by Telste (1989). He uses a similar method but applies a damping layer at the edge of his computational domain to model an infinite horizontal extent. His results for Froude numbers 7.07, 2.24, and 0.5 and initial vortex depth five times the vortex separation, agree well with what would be expected from the simulations presented here. Telste generally found energy to be well conserved for the time he simulated.

As a model of real flows, point vortices have several well-known short-comings. To account for a more realistic situation, we have repeated our calculations using both finite area vortex regions and vortex sheets to represent the vortical flow. Calculations for the evolution of an initially flat vortex sheet with a vortex sheet strength corresponding to an elliptic lift distribution are shown in figures 26 to 28. The Froude number is based on the separation that the vortices would have in the absence of a free surface, estimated by assuming that the sheet will become a pair of point vortices. The free surface and the vortex sheet are discretized by 200 points each, and we use a relatively large vortex blob radius, δ equal to 0.5 times the separation between the vortices, for the vortex sheet (Several of our vortex sheet runs have been repeated with different blob radii to check that the effect of finite δ is minimal and confined to the vortex cores.).

In figure 26, the Froude number is 11.2, the same as in figure 18. The vortex sheet rolls up quickly into two counter-rotating vortices that collide with the free surface much in the same way as the point vortices did in figure 18. The vortex points are connected by straight line segments, except when they have moved very far apart.

Therefore, in figure 26 and subsequent figures, (as well as in figure 17), the line is not continuous in regions where the sheet undergoes large stretching. Vortices generated from a vortex sheet with elliptic loading have a rather "peaked" vorticity distribution (the vortex sheet strength is maximum at the ends of the sheet); therefore, it is not surprising that the results are virtually identical to the point vortex case (figure 18). Figure 27 shows the evolution for the same Froude number as figure 19, 3.54. The evolution is clearly in the transition zone and is similar to figure 19. In figure 28 the Froude number is 1.58, as in the point vortex case in figure 20. Again, the differences are quite small. Simulations for smaller Froude number show the same behavior as observed in the point vortex case, namely, the interaction pattern is relatively unchanged, but the amplitude is decreases.

The vortex sheet strength distribution used here leads to a rather concentrated vorticity distribution, once the roll-up is completed. To investigate a "flatter" vorticity distribution we have repeated the calculations modeling the vortices as vortex patches, or finite area vortex regions (FAVR's). There is now an additional geometric length scale, namely, the size of the vortex patch. In figure 27a, the vortices are initially circular regions with a diameter 0.45 times their separation distance and centers at a depth equal to 1.25 their separation (the same as for the point vortices and the vortex sheet). The free surface is discretized by 300 computational elements, and the bounding curve of each vortex is discretized by 100 elements. As the vortices move upward, they deform and acquire a somewhat elongated shape, as observed for a pair of FAVR's moving in unbounded fluids (Overman and Zabusky (1982)). While the overall evolution is the same as in figures 18 and 26, the large-amplitude stage exhibits some differences. The neck of the blob is narrower, and the blob is both wider and taller. The same setup for a smaller patch diameter, 0.3, is shown in figure 29b. The large-amplitude stage is now more like the point vortex and the vortex sheet cases. In figure 30, $Fr = 3.54$, as in figures 19 and 27, and the diameter is 0.45 times the

separation in (a) and 0.3 in (b). Relatively good correlation with the point vortex and vortex sheet calculations is observed in both cases, in particularly for the smaller patch radius. Figure 31 shows the evolution for $Fr = 1.58$ and the diameter is 0.45. The surface deformation is similar to the point vortex and vortex sheet cases (figures 20 and 28), but the depth of the trough is slightly smaller.

To compare the three models quantitatively, we have monitored the same information as was presented for the point vortex runs. In figure 32 we show the maximum and minimum elevation versus time in (a), and the path of the vortices in (b). For the vortex sheet and the FAVR model, the path of the center of vorticity is plotted. While the run with the large FAVR's initial conditions (figure 31) shows a slight deviation, (for example, making an earlier turn than the other vortices in figure 32), the results for all models are in close agreement.

As in the previous section we investigated the effect of surface tension on a single case. Figure 33 compares the late time stage ($t = 9.8$) of two simulations with the calculation in figure 18; for curve (a) Weber number is infinite, for (b) $We = 0.33$, and for (c) $We = 1.0$. The increased amount of surface tension reduces the growth of the surface deformation and leads to a larger separation of the vortices. For even smaller Weber number, the surface deformation is largely inhibited, but several short waves appear on the surface. These waves could be capillary waves, but we have not ruled out numerical difficulties as a cause. Large surface tension results in a very stiff system, and minute time steps are necessary.

We conclude this section by examining the collision of a vortex pair generated by a vortex sheet initially inclined with respect to the free surface (figure 34). The vortices collide now with the surface at an angle, and the main surface deformation is due to the vortex that first encounters the surface. As the first vortex interacts with the surface, the other continues to propagate, causing the line connecting the vortices to become more aligned with the surface. The resulting deformation is similar to that of

a single vortex interacting with the surface, observed in the previous section, and will not be discussed in detail. In these particular calculations, the surface deformation leads to a breaking wave and the calculation could not be continued. We expect that at a later stage, both vortices would align with the surface, and the subsequent development would be more like that in the head-on collision problem.

For most of the simulations discussed in this report we have monitored several additional parameters, that might be of interest in detailed comparisons with experimental data, such as the surface slopes, surface velocities, and upwelling of fluids with the vortex pairs. Generally, we find that while such data provides some additional insight into the problem, the qualitative trend is obvious from the solution plots, and the data we have presented. Thus, we will postpone the presentation of these diagnostics until experimental data is available for comparison. Preliminary comparisons have been presented in Willmarth, Tryggvason, Hirt and Yu (1989).

4. Conclusions

For remote sensing, which provides the motivation for this study, the most important question is, How much can we tell about the submerged vortical flow from observations of the free surface? Though it is likely that a complete solution to this inverse problem does not exist, the Froude number obviously has a great influence on the free surface and the vortex motion. In the vortex collision problem, the Froude number was the main controlling parameter, and the geometric parameters such as the initial relative depth and the core size appeared to play minor roles (at least for the cases that we investigated). For the shear layer problem, there was an additional controlling parameter, the relative depth. This parameter could have been eliminated by considering an infinitely long domain; indeed for the relatively shallow flows the boundaries of the domain do not seem to influence the evolution significantly, except for the largest Froude numbers. Generally, it appears that the free surface deformation is representative of the vortex motion only for large Froude numbers. In that limit the vortices initially push the free surface as if it was a passive marker; however, the result is a large surface deformation that eventually affects the path of the vortices. For the small Froude number limit, the vortices interact with the surface much as if it was a rigid wall, the surface deformation is much smaller (and decreases rapidly with Froude number), more localized, and the length scale of the surface deformation is much smaller than those of the vortical flow. In addition, at low Froude numbers, there is considerable difference between the surface signature of a transient vortical motion (for example, the impulsively started vortex) and that of an essentially steady-state flows.

One purpose of our study was to investigate the dependence of surface deformation on the detailed nature of the vortex modeling. As might be expected, in those cases where the flow evolution is not sensitive to the model, the surface deformation is also minimally affected, but when the vortex evolution depends strongly on the model, the

surface deformation also relies on the model. Therefore, for the shear layer problem, considerable dependence was observed, but the vortex collision problem was relatively insensitive to whether we used points, sheets, or patches to model the vorticity.

This study presents our first step in an effort to develop a comprehensive understanding of the free surface signature of submerged, unsteady vortical flows. The flows considered here are therefore relatively simple, and we conclude with a few remarks about the limitations of this present study, and what we are doing about these limitations.

The most restrictive assumption, presumably, is that we have confined our attention to two-dimensional models. While such models are of relevant to certain experimental situations and produce considerable insight into some of the interaction mechanisms, most of the vortex interactions observed experimentally involve fully three-dimensional motions. In Sarpkaya's (1988) and Willmarth and Hirs'a's (1988) experiments on the surface signature of trailing vortices, for example, the appearance of striations is a three-dimensional phenomena. Furthermore, in Bernal's experiments with sub-surface jets (Bernal and Madnia (1988)) and vortex rings (Bernal and Kwon (1988)), the predominant wave-making mechanism is the "opening up" of vortex rings colliding obliquely with the surface. We have recently completed a fully three-dimensional boundary integral method for free surface flows and have run preliminary studies with simple vortex models such as a circular vortex filament. Although these preliminary studies show promising correlation with the experimentally observed phenomena, a considerable amount of refinement is still needed.

Another complication is the presence of surface contaminants on real free surfaces. Generally, the surface motion created by vortical flow results in an uneven distribution of the contaminants and thus non-uniform surface tension. While the effect of surface contaminants on the damping of surface waves is reasonably well understood, the effects on vortical structures below the free surface have received much

less attention. Baker and Crow (1977) observed that a vortex pair colliding with the surface produced secondary vortices and rebounded, as when vortices collide with a rigid surface. Saffman (1979) pointed out that for inviscid flow and a flat boundary, rebounding can not occur and suggested that the behavior might be due to surface tension effects. On the basis of numerical simulations, Peace and Riley (1983) argued that even for stress-free boundaries viscosity would cause rebounding. However, their calculation was for rather low Reynolds numbers, and with increasing Reynolds number, the rebounding decreased significantly.

Willmarth and collaborators recently addressed surface tension effects on vortical flow experimentally, and demonstrated a rather dramatic dependence on the cleanness of the surface. For a clean surface, the vortical motion behaves as would be expected from an inviscid analysis (If the surface deforms, some rebounding is predicted, see figure 32, but most of the experiments have been performed under conditions where surface deformation are minimal.). But in the presence of surface contamination, the shear stress induced by uneven surface tension results in considerable vorticity production, and subsequent boundary layer separation whereby this vorticity is swept into the interior. As Willmarth notes, this injection of vorticity and its subsequent interaction with the primary vorticity appears to be the leading effect of the surface contaminants.

While our inviscid method is easily modified to account for constant surface tension (figures 16 and 33) and can easily predict the redistribution of a surface contaminant, the resulting shear stress is incompatible with the inviscid model. We have investigated the possibility of coupling our method with a simple boundary layer model at the surface, and while such modeling is relatively straightforward, it does not account for the injection of vorticity through separation. It is not obvious how such mechanism can (or should!) be incorporated into a vortex model, and we (in collaboration with Willmarth) as well as Dr. R. Leighton at the NRL (private communication)

are currently conducting investigations using the full Navier-Stokes equation. Such studies, although limited to relatively low Reynolds numbers, are expected to shed more light on this matter.

Acknowledgment.

This work was supported under the Program in Ship Hydrodynamics (PSH) at the University of Michigan, funded by the University Research Initiative of the Office of Naval Research, (contract No. N000184-86-K-0684) and by NSF grant MSM-8707646. Constructive interaction with professors W. W. Willmarth, W.J.A. Dahm, L. Bernal, and other member of the PSH has been most helpful in carrying out the research discussed here. The calculations were done mostly on the computers at the San Diego Supercomputer Center, which is sponsored by the NSF.

References

- Baker, G. R., Meiron, D. I. and Orszag, S. A. 1982. Generalized vortex methods for free surface flow problem. *J. Fluid Mech.* **123**, 477-501.
- Baker, S. J. and Crow, S. C. 1977. The motion of two-dimensional vortex pairs in a ground effect. *J. Fluid Mech.* **82**, 659-671.
- Bernal, L. P. and Madnia, K. 1988. Interaction of a turbulent round jet with the free surface. *Proceedings of 17th Symposium on Naval Hydrodynamics*, Aug. 29-Sep. 2, The Hague, The Netherlands. In press (National Academy of Science, Washington, 1989).
- Bernal, L. P. and Kwon, J. T. 1989. Vortex ring dynamics at a free surface. *Phys. Fluids A*, **1**, 449-451.
- Dahm, W. J. A., Scheil, C. M. and Tryggvason, G. 1989. Dynamics of vortex interaction with a density interface. *J. Fluid Mech.* (to appear)
- Dold, J. W. and Peregrine, D. H. 1986. An efficient boundary-integral method for steep unsteady water waves. In *Numerical Methods for Fluid Dynamics II*, eds. Morton, K. W. and Bains, M. J., Oxford U. P., 671-679.
- Hogan, S. J. 1981. Some effects of surface tension on steep water waves. *J. Fluid Mech.* **110**, 384-410.
- Hong, S. W. 1987. Unsteady separated flow around a two-dimensional bluff body near a free surface. *Ph.D. Thesis*. The University of Michigan.
- Kochin, N. E., Kibel, I. A., and Roze, N. V. 1964. *Theoretical Hydrodynamics*. Interscience, New York.
- Krasny, R. 1986. Desingularization of periodic vortex sheet roll up. *J. Comput. Phys.* **65**, 292-313.

- Krasny, R. 1988. Computation of vortex sheet roll-up in the Trefftz plane. *J. Fluid Mech.* **184**, 123-155.
- Lamb, H. 1945. *Hydrodynamics*. Dover Publication, New York, 738 pages.
- Leonard, A. 1980. Vortex methods for flow simulation. *J. Comput. Phys.* **37**, 289-335.
- Longuet-Higgins, M. S. and Cokelet, E. D. 1976. The deformation of steep surface waves on water. II. Growth of normal-mode instabilities. *Proc. Roy. Soc. Lond. A* **364**, 1-28.
- Lugt, H. J. 1981. Numerical modeling of vortex flows in ship hydrodynamics. *Third International Conference on Numerical Ship Hydrodynamics*, 297-317.
- Lugt, H. J. 1983. *Vortex Flow in Nature and Technology*. Wiley, New York, 297 pages.
- Marcus, D. L. 1988. The interaction between a pair of counter-rotating vortices and a free boundary. *Ph.D. Thesis*. The University of California at Berkeley.
- Novikov, YE. A. 1981. Generation of surface waves by discrete vortices. *Izvestiya, Atmospheric and Oceanic Physics* **17**, 709-714.
- Overman, E. A. and Zabusky, N. J. 1982. Coaxial scattering of Euler-equation translating V-states via contour dynamics. *J. Fluid. Mech.* **125**, 187-202.
- Peace, A. J. and Riley, N. 1983. A viscous vortex pair in ground effect. *J. Fluid Mech.* **129**, 409-426.
- Pozrikidis, C. and Higdon, J. J. L. 1985. Nonlinear Kelvin-Helmholtz instability of a finite vortex layer. *J. Fluid Mech.* **157**, 225-263.

- Pullin, D. I. 1982. Numerical studies of surface-tension effects in non-linear Kelvin-Helmholtz and Rayleigh-Taylor instability. *J. Fluid Mech.* **119**, 507-532.
- Saffman, P. G. 1979. The approach of a vortex pair to a plane surface in inviscid fluid. *J. Fluid Mech.* **92**, 497-503.
- Sarpkaya, T. 1986. Trailing-vortex wakes on the free surface. *16th Symposium on Naval Hydrodynamics*, National Academy Press, 38-50.
- Sarpkaya, T., Elnitsky II, J., and Leeker Jr., R. E. 1988. Wake of a vortex pair on the free surface. *Proceedings of 17th Symposium on Naval Hydrodynamics*, Aug. 29-Sep. 2, The Hague, The Netherlands.
- Sarpkaya, T. 1989. Computational methods with vortices—the 1988 freeman scholar lecture. *ASME, J. of Fluids Eng.*, **111**, 5-52.
- Saunders, H. E., 1965. Hydrodynamics in ship design. Vol. III, *SNAME*.
- Schultz, W. W., 1987. A complex-valued integral method for free surfaces with intersecting bodies. *Second International Workshop on Water Waves and Floating Bodies*, Bristol, England.
- Shanpine, L. F. and Gordon, M. K. 1965. *Computer solution of ordinary differential equations*. Freeman.
- Song, M., Yu, D. and Tryggvason, G. 1988. Vortex interaction with a free surface. *Bull. Am. Phys. Soc.* **33**, 2279. (abstract only).
- Telste, J. H. 1989. Potential flow about two counter-rotating vortices approaching a free surface. *J. Fluid Mech.* (to appear).

- Tryggvason, G. 1988a. Vortex dynamics of stratified flows. *Proceedings of the SIAM Workshop on Mathematical Aspects of Vortex Dynamics*, Leesburgh, Virginia, April 25-27.
- Tryggvason, G. 1988b. Deformation of a free surface as a result of vortical flows. *Phys. Fluids* **31**, 955-957.
- Tryggvason, G. 1989. Simulation of vortex sheet roll-up by vortex methods. *J. Comput. Phys.* **80**, 1-16.
- Vinje, T. and Brevig, P. 1981. Numerical simulation of breaking waves. *Adv. Water Resources* **4**, 77-82.
- Wehausen, J. V. and Laitone E. V. 1960. Surface waves. *Encyclopedia of Physics*, Springer, Berlin, Vol. IX, 446-778.
- Willmarth, W. W. and Hirska, A. 1988. Personal communications.
- Willmarth, W. W., Tryggvason, G., Hirska, A. and Yu, D. 1989. Vortex pair generation and interaction with a free surface. *Phys. Fluids A* **1**, 170-172.
- Zabusky, N. Y., Hughes, M. H. and Roberts, K. V. 1979. Contour dynamics for the Euler equations in two dimensions. *J. Comput. Phys.* **30**, 96-106.

Figure Caption

Figure 1: The evolution of a free surface and a submerged vortex sheet with $Fr = 0.5$, $d/L = 0.2$, $\delta = 0.1$, $N_{surface} = 200$, $N_{vortex} = 200$. The nondimensional times shown are 0.0, 0.5, 1.00, 1.25, 1.4.

Figure 2: The large-amplitude stage of a free surface and a submerged vortex sheet with $Fr = 0.5$, $d/L = 0.2$. The nondimensional time shown is 1.4. (a): $\delta = 0.1$, $N_{surface} = 200$, $N_{vortex} = 200$. (b): $\delta = 0.2$, $N_{surface} = 200$, $N_{vortex} = 200$. (c): $\delta = 0.2$, $N_{surface} = 50$, $N_{vortex} = 50$.

Figure 3: A large-amplitude stage for various values of the nondimensional parameters with $N_{surface} = 200$, $N_{vortex} = 300$. (a): $Fr = 1.0$, $d/L = 0.2$. (b): $Fr = 1.0$, $d/L = 0.3$. (c): $Fr = 1.0$, $d/L = 0.4$. (d): $Fr = 0.5$, $d/L = 0.2$. (e): $Fr = 0.5$, $d/L = 0.3$. (f): $Fr = 0.5$, $d/L = 0.4$. (g): $Fr = 0.354$, $d/L = 0.2$. (h): $Fr = 0.354$, $d/L = 0.3$. (i): $Fr = 0.354$, $d/L = 0.4$. (j): $Fr = 0.25$, $d/L = 0.2$. (k): $Fr = 0.25$, $d/L = 0.3$. (l): $Fr = 0.25$, $d/L = 0.4$. The nondimensional times are approximately 1.25 for the first column, 1.6 for the second one, and 2.0 for the third one..

Figure 4: The free surface profiles for a few cases from figure 3. Figures 3 g to i are amplified 5 times and figures j to l are amplified 10 times in the vertical dimension. The letters correspond to figure 3.

Figure 5 (a): The total amplitude, $Y_{max} - Y_{min}$, versus time for the cases in figure 3. (b): The location of the maximum surface depth, X_{min} , versus time for the runs in figure 3. (c): a_1 for the runs in figure 3 versus time. (d): θ_1 for the runs in figure 3 versus time.

Figure 6 (a): The position of the vortex center for the runs in figures 3a and 3l versus time. (b): The second moments of the vortex sheet for the runs in figures 3a and 3l versus time.

Figure 7: The evolution of a free surface and a shear layer of the finite thickness, $N_{surface} = 200$, $N_{vortex} = 400$. (a): $d/L = 0.2$, $Fr = 1.0$, and $t/L = 0.1$. The nondimensional times are 0.0, 0.9, 1.5, 2.0. (b): $d/L = 0.2$, $Fr = 1.0$, and $t/L = 0.15$. The nondimensional times are 0.0, 1.0, 1.5, 2.4.

Figure 8: The large-amplitude stage of a free surface and shear layer of finite thickness, $N_{surface} = 200$, $N_{vortex} = 400$. (a): $d/L = 0.3$, $Fr = 0.5$, and $t/L = 0.1$. The nondimensional time is 1.75. (b): $d/L = 0.3$, $Fr = 0.5$, and $t/L = 0.15$. The nondimensional time is 2.4

Figure 9: The large-amplitude stage of a free surface and shear layer of the finite thickness, $N_{surface} = 200$, $N_{vortex} = 400$. (a): $d/L = 0.4$, $Fr = 0.354$, and $t/L = 0.1$. The nondimensional time is 2.1. (b): $d/L = 0.4$, $Fr = 0.354$, and $t/L = 0.15$. The nondimensional time is 3.0.

Figure 10 (a): a_1 for the runs in figures 4, 8, 9 and 10 versus time. (b): θ_1 for the runs in figures 4, 8, 9 and 10 versus time.

Figure 11: The evolution of a free surface for the point vortex model with $d/L = 0.2$, $Fr = 1.0$. The nondimensional times are 0.0, 0.17, 0.27, 0.4, 0.51.

Figure 12: The evolution of a free surface for the point vortex model with $d/L = 0.3$, $Fr = 0.5$. The nondimensional times are 0.0, 0.48, 0.69, 0.78.

Figure 13: The evolution of a free surface for the point vortex model with the $d/L = 0.05$, $Fr = 10^{-4}$. The nondimensional times are 0.0, 1.0, 2.0, 3.0, 4.0. The vertical dimension is enlarged 200 times, except for the top frame.

Figure 14: A comparison of the linearized solution with our numerical calculation. $Fr = 1.22 \times 10^{-9}$, $d/L = 0.005$. (a): $N = 600$, and nondimensional time equals 0.235. (b): $N = 300$, and nondimensional time equals 0.295. (c): $N = 600$, and $N = 300$,

and non-dimensional time is equal to 0.42. In (a) and (b) the short time solution, eq. 3.4, is used.

Figure 15: The propagation of a capillary wave. (a): Wave speed. Solid line is the prediction by linear theory, the dots are numerical calculations with $\lambda/\lambda_m = 0.151, 0.302, 1.004, 1.92, 3.33$. (b): Profile for $\lambda/\lambda_m = 1.92$. Solid line is the initial profile. Dashed line compares the profile at $t = 1.25$ as predicted by linear theory and computations.

Figure 16: The effect of surface tension on the large-amplitude stage for $d/L = 0.2$, and $Fr = 1.0$ at the nondimensional time 1.25. The solid line is for $We = 0.33$, long dashed line is for $We = 1$, and the dashed line is the infinite Weber number solution from figure 3a.

Figure 17: The surface signature of vortex pairing. $Fr = 1.0$, and $d/L = 0.3$. The nondimensional times are 0.0, 0.5, 1.0, 1.5, 2.0, 2.5.

Figure 18: Collision of a pair of point vortices with a free surface. $d/L = 1.25$, $Fr = 11.2$ and $N_{surface} = 200$. The nondimensional times are 0.0, 3.0, 6.0, 9.0, and 10.5.

Figure 19: Collision of a pair of point vortices with a free surface. $d/L = 1.25$, $Fr = 3.54$ and $N_{surface} = 200$. The nondimensional times are 0.0, 3.0, 6.0, 9.0, and 10.5.

Figure 20: Collision of a pair of point vortices with a free surface. $d/L = 1.25$, $Fr = 1.58$ and $N_{surface} = 200$. The nondimensional times are 0.0, 3.0, 6.0, and 9.0.

Figure 21: The late time for the interaction of a point vortex pair with a free surface, $d/L = 1.25$, and $N_{surface} = 200$. (a): $Fr = 11.2$, (b): $Fr = 15.8$, (c): $Fr = 22.4$, (d): $Fr = 0.50$, (e): $Fr = 0.79$, (f): $Fr = 1.54$. The nondimensional time is 10.0 in (a), (b), and (c) and 9.0 in (d), (e), and (f).

Figure 22(a): The maximum and minimum of the amplitude of the free surface for the runs in figures 18, 19, and 20 versus time. (b): The potential energy for the runs in figures 18, 19, and 20 versus time. Lines a, b, and c represent the runs in figures 18, 19, and 20 respectively.

Figure 23: The path of the point vortices for the runs in figures 18, 19, and 20 versus time. The distance between the dots on each line marks a time interval of 1. Lines a, b, and c represent the runs in figures 18, 19, and 20 respectively.

Figure 24: The dependency of the solution on the box size at $t = 9.25$ for $d/L = 1.25$, and $Fr = 11.2$. The box sizes are 0.67, 1.0, and 1.34. The number of the points on the free surface is 200.

Figure 25: The potential energy, kinetic energy, and total energy versus time for $d/L = 1.25$, $Fr = 11.2$ with $N_{surface} = 200$. The straight horizontal line is for reference.

Figure 26: The collision of a vortex pair formed from a vortex sheet with a free surface. $d/L = 1.25$, $Fr = 11.2$ and $N_{surface} = 200$, $N_{vortex} = 200$. The nondimensional times are 0.0, 3.0, 6.0, 9.0 and 10.5.

Figure 27: The collision of a vortex pair formed from a vortex sheet with a free surface. $d/L = 1.25$, $Fr = 3.54$ and $N_{surface} = 200$, $N_{vortex} = 200$. The nondimensional times are 0.0, 3.0, 6.0, 9.0 and 10.5.

Figure 28: The collision of a vortex pair formed from a vortex sheet with a free surface. $d/L = 1.25$, $Fr = 1.58$ and $N_{surface} = 200$, $N_{vortex} = 200$. The nondimensional times are 0.0, 3.0, 6.0, 9.0 and 10.5.

Figure 29: The collision of a finite area vortex pair with a free surface. (a): $d/L = 1.25$, $Fr = 11.2$, $di/L = 0.45$ and $N_{surface} = 200$, $N_{vortex} = 200$. The nondimensional times are 0.0, 3.0, 6.0, 9.0 and 10.5. (b): $d/L = 1.25$, $Fr = 11.2$, $di/L = 0.3$ and

$N_{surface} = 200$, $N_{vortex} = 200$. The nondimensional times are 0.0, 3.0, 6.0, 9.0 and 10.5.

Figure 30: The collision of a finite area vortex pair with a free surface. (a): $d/L = 1.25$, $Fr = 3.54$, $d_i/L = 0.45$ and $N_{surface} = 200$, $N_{vortex} = 200$. The nondimensional times are 0.0, 3.0, 6.0, 9.0 and 10.5. (b): $d/L = 1.25$, $Fr = 3.54$, $d_i/L = 0.3$ and $N_{surface} = 200$, $N_{vortex} = 200$. The nondimensional times are 0.0, 3.0, 6.0, 9.0 and 10.5.

Figure 31: The collision of a finite area vortex pair with a free surface. $d/L = 1.25$, $Fr = 1.58$, $d_i/L = 0.45$ and $N_{surface} = 200$, $N_{vortex} = 200$. The nondimensional times are 0.0, 3.0, 6.0 and 9.0.

Figure 32: (a): The maximum and minimum elevation versus time: the first frame is for the runs in figures 26 and 29, the second for the runs in figures 27 and 30, and the third for the runs in figures 28 and 31. (b): The path of the center of vorticity versus time: the first frame is for the runs in figures 26 and 29, the second for the runs in figures 27 and 30, and the third for the runs in figures 28 and 31.

Figure 33: A comparison of the evolution of a free surface with $We = 3.0$, $We = 1.0$ and infinite Weber number for $Fr = 11.2$. Nondimensional time is 9.8.

Figure 34: The evolution of a free surface due to a collision of a vortex pair with an angle of 45° , average $d/L = 0.88$, $Fr = 3.54$, $N_{surface} = 200$, $N_{sheet} = 200$. The nondimensional times are 0.0, 2.4, 4.3, 5.1, 6.7.

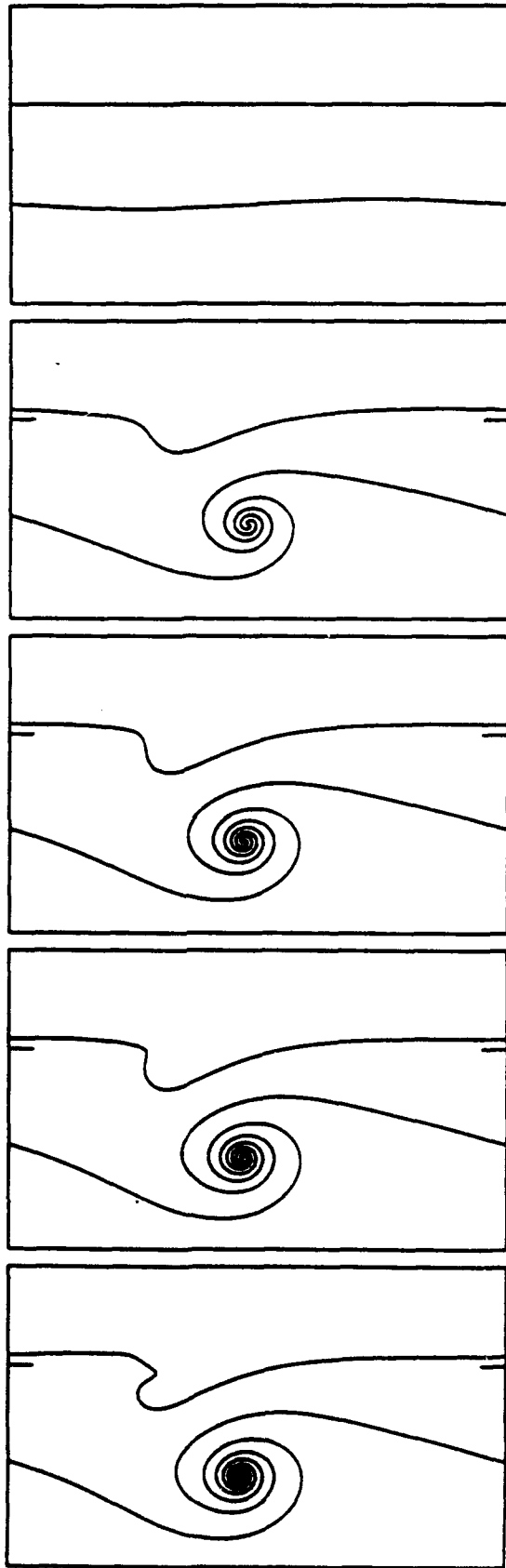
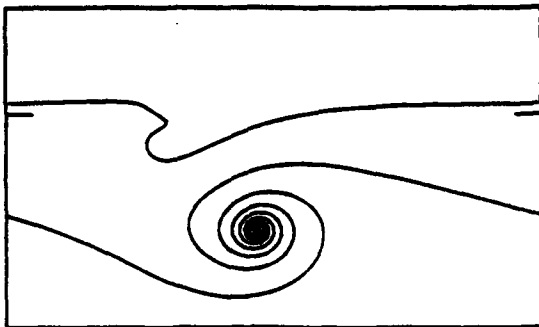
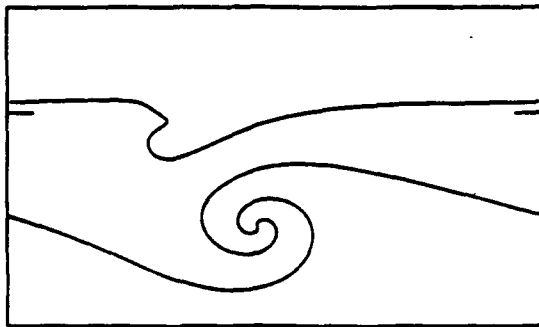


Fig. /

(a)



(b)



(c)

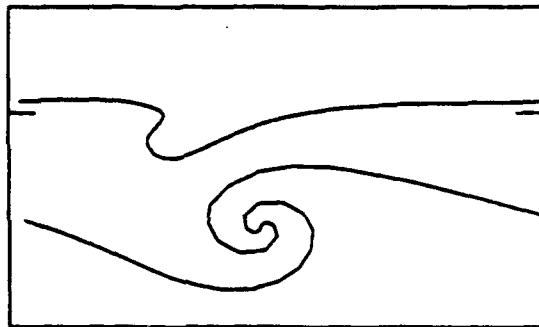
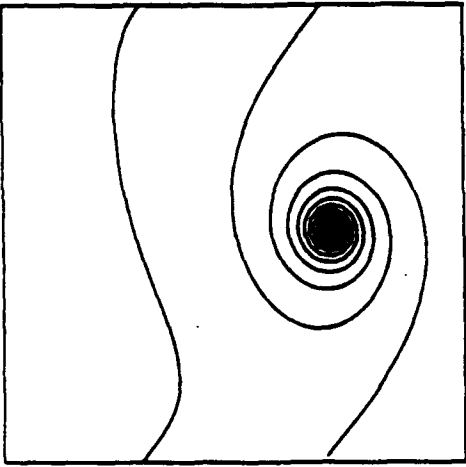
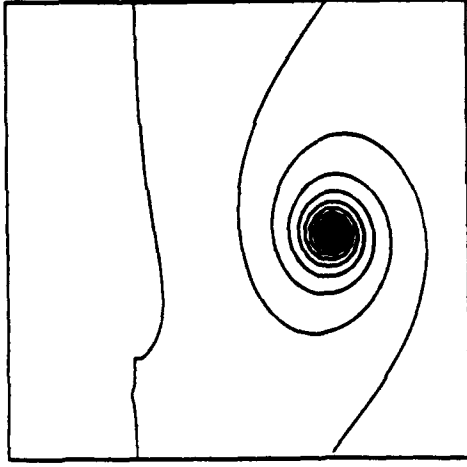


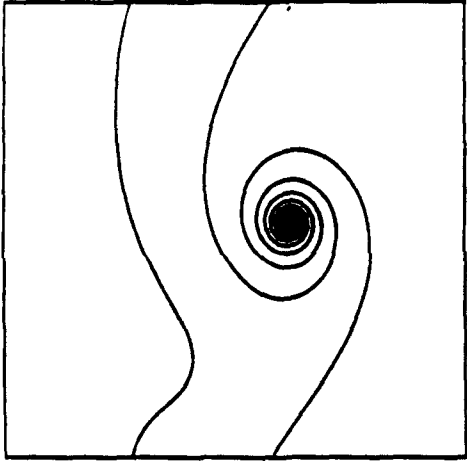
Fig. 2



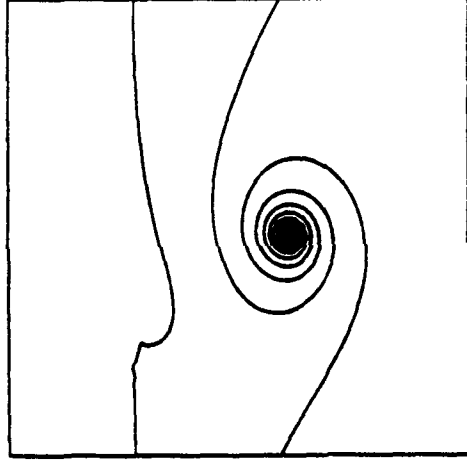
c



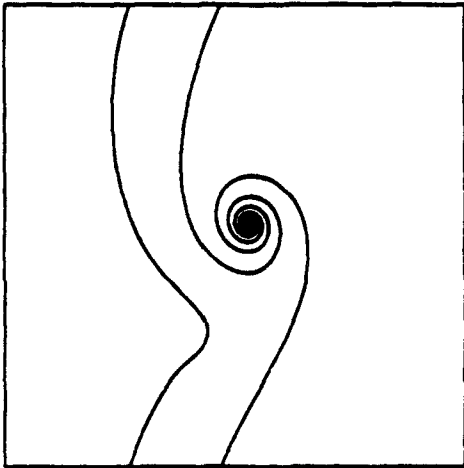
f



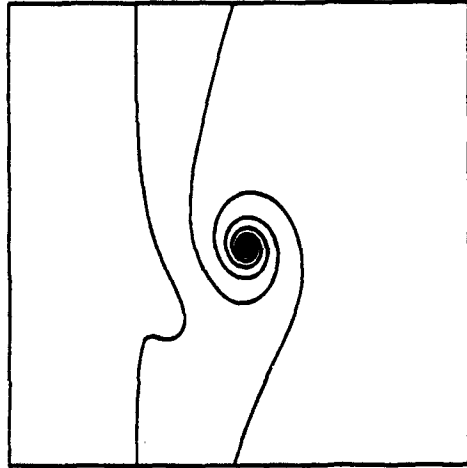
b



e

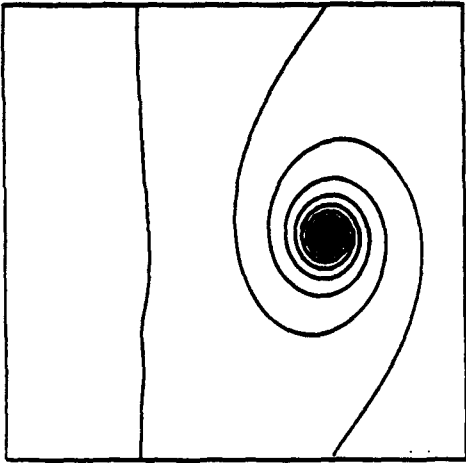


a

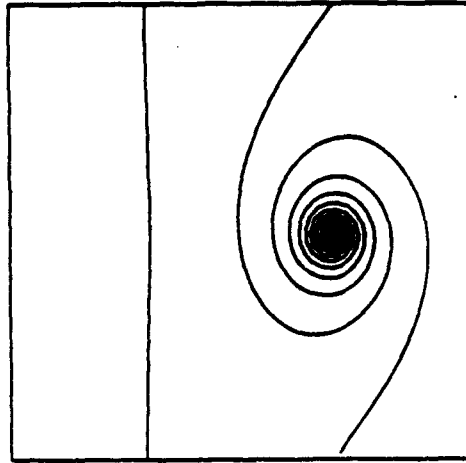


d

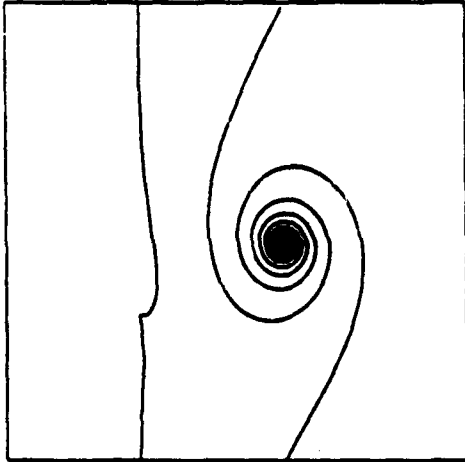
Fig 3



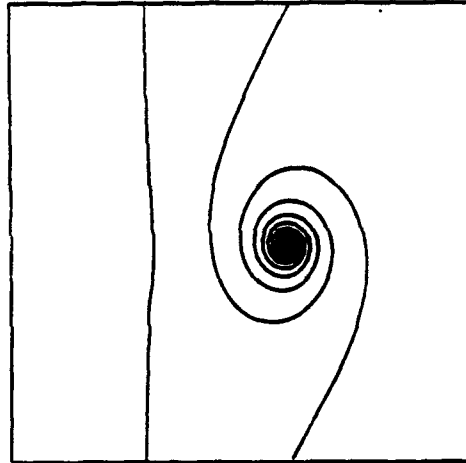
i



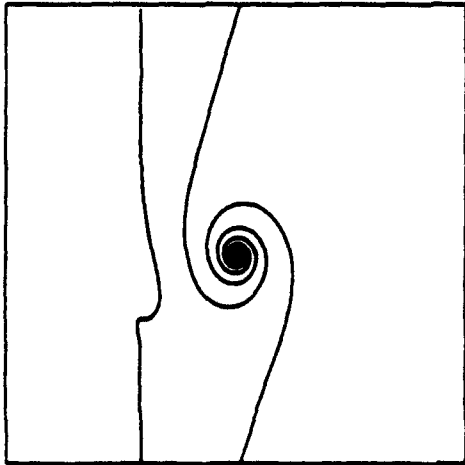
i



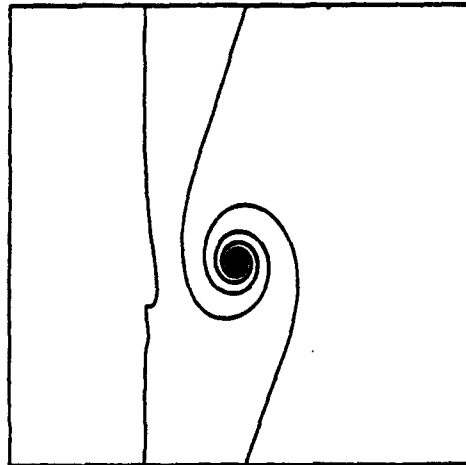
h



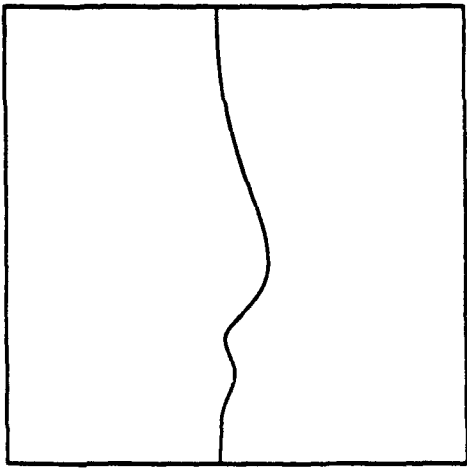
k



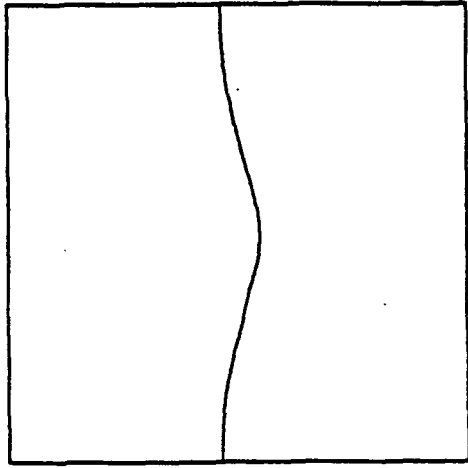
g



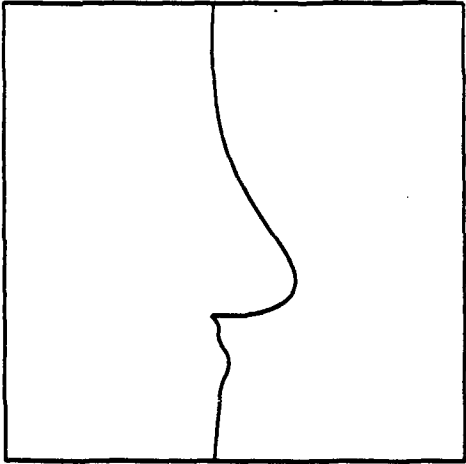
j



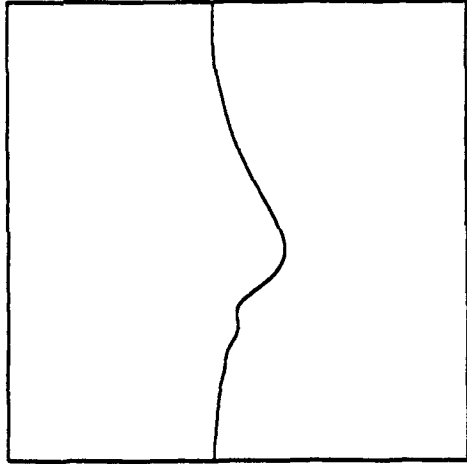
i



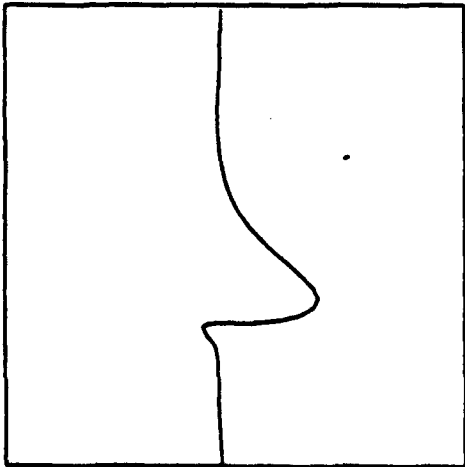
l



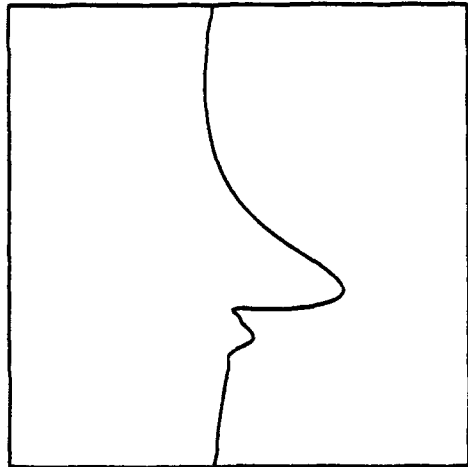
h



k

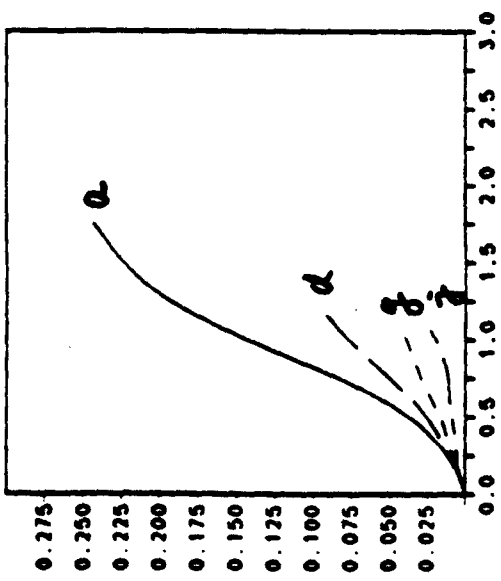
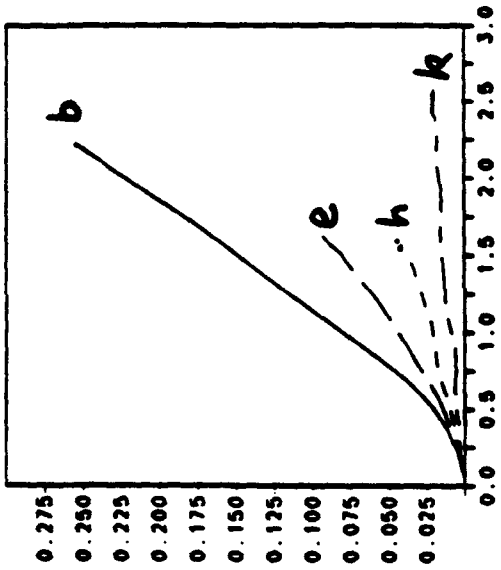
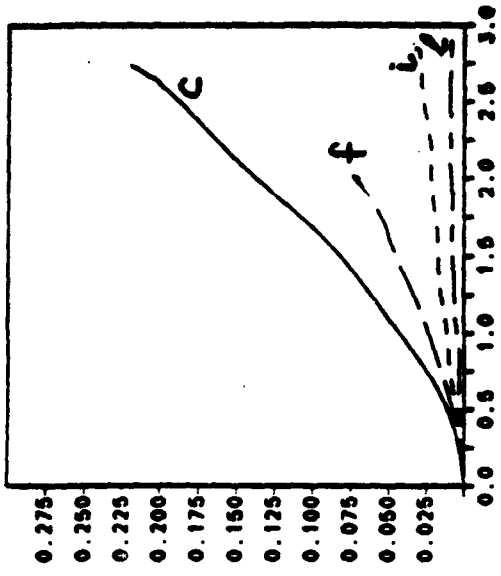


g

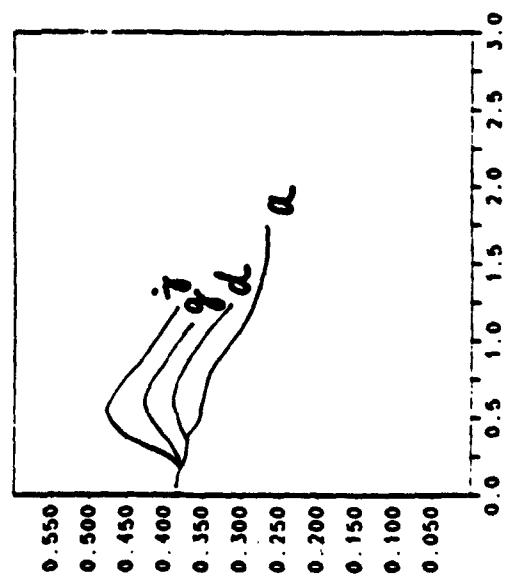
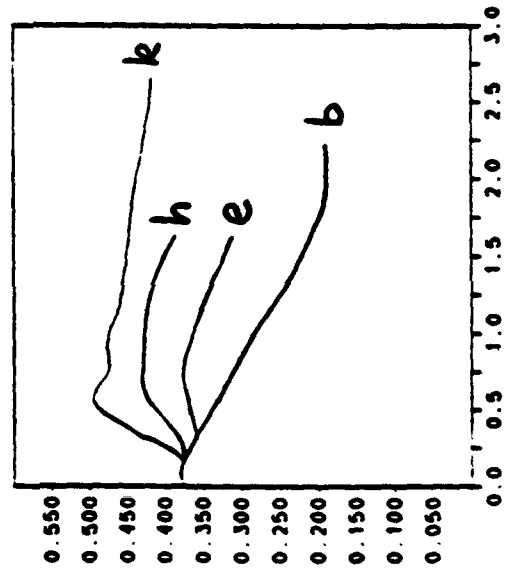
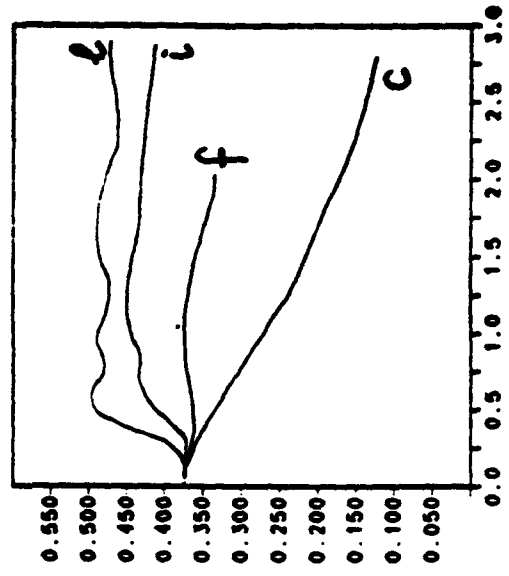


j

Fig 4

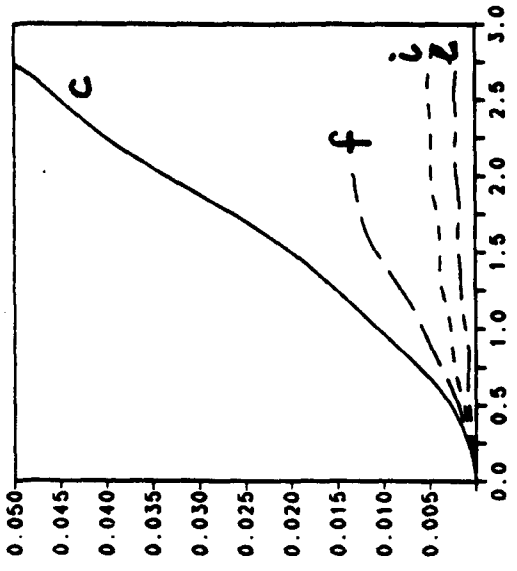
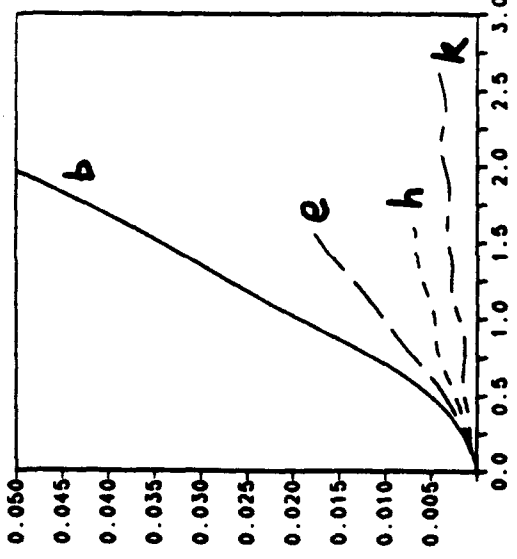
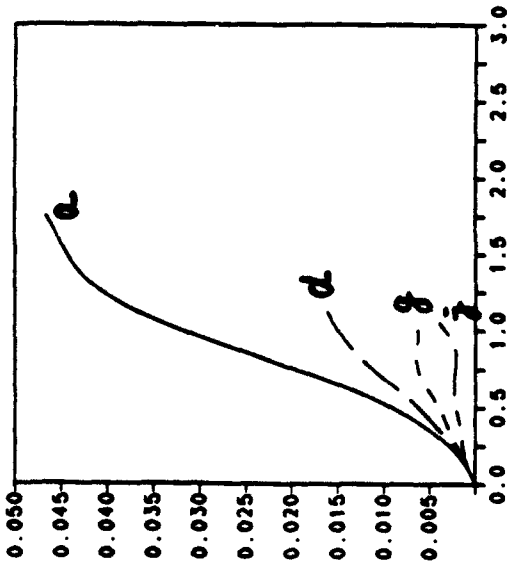


(a)

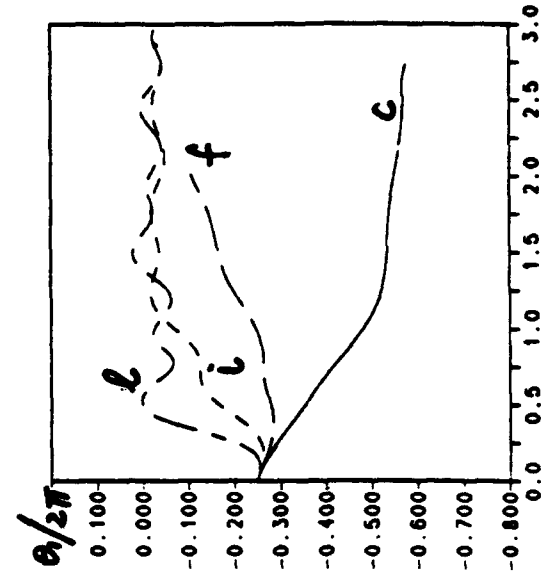
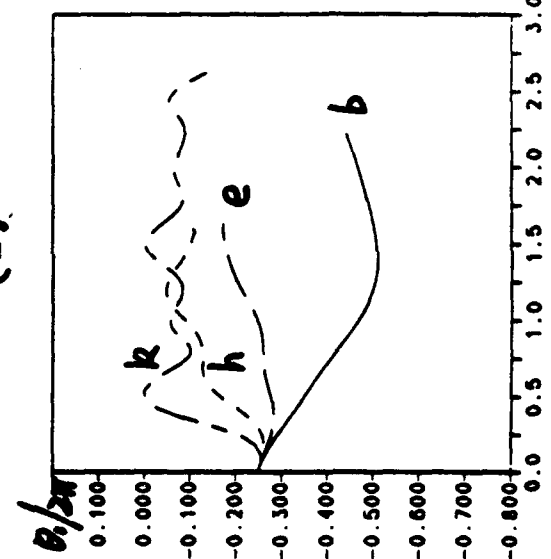
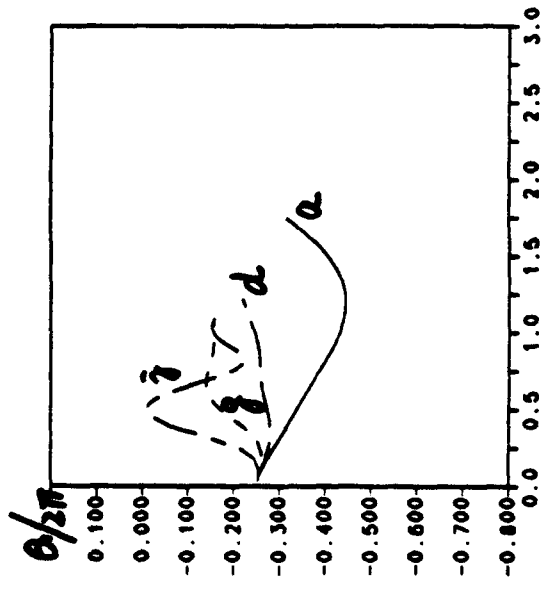


(b)

Fig 5



(c)



(d)

Fig 5 cont.

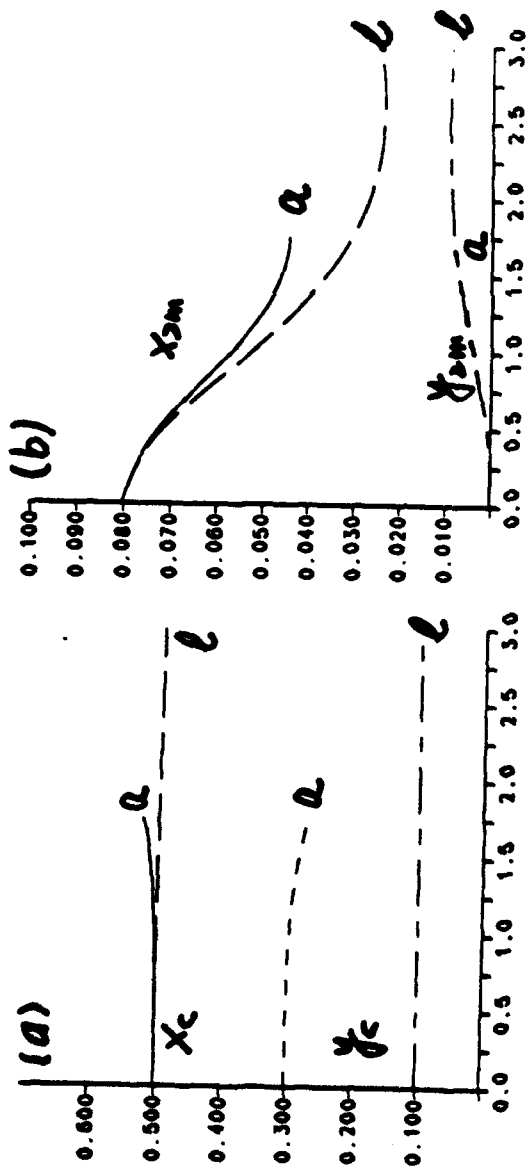
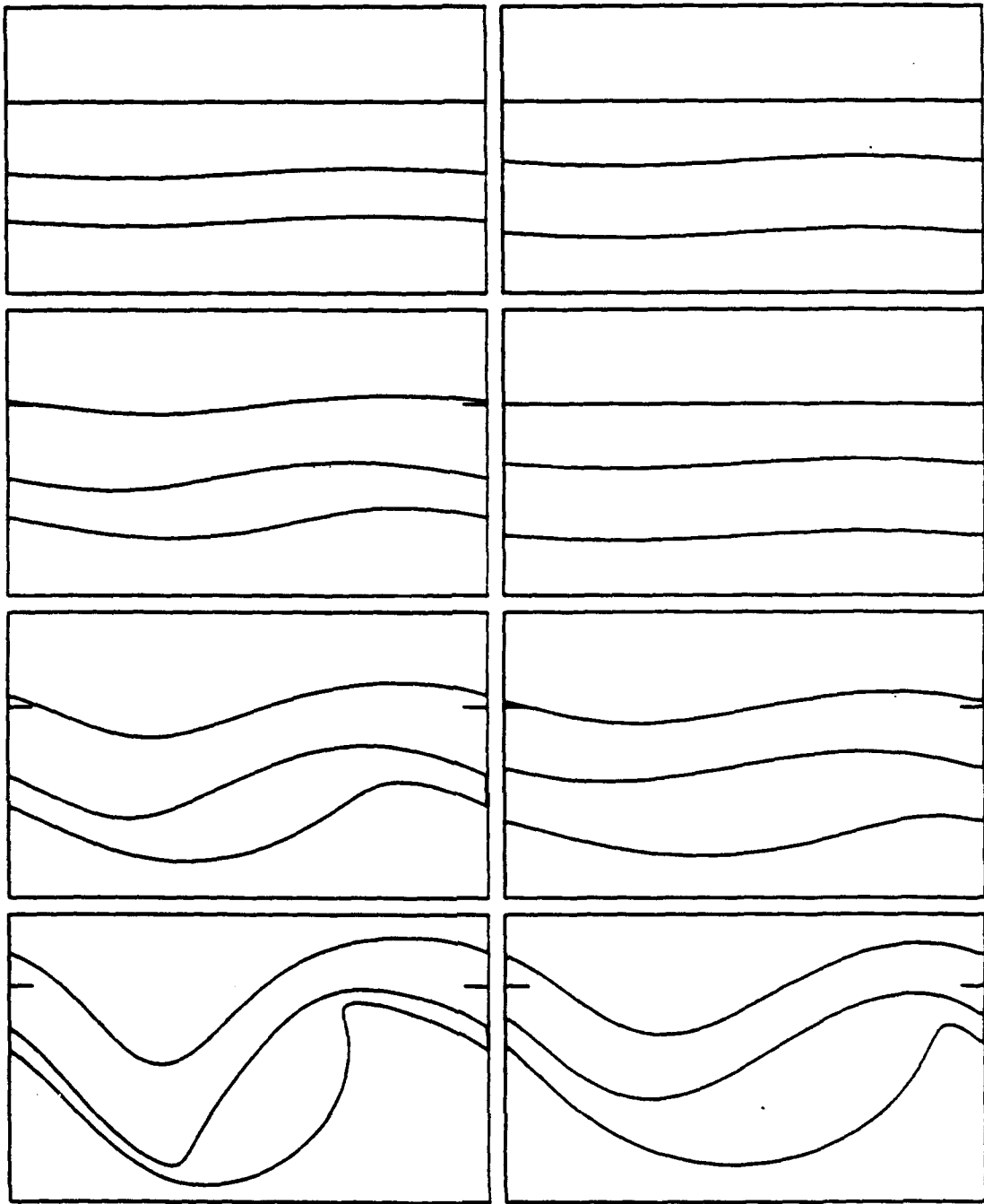


Fig 6



(a)

(b)

Fig. 7

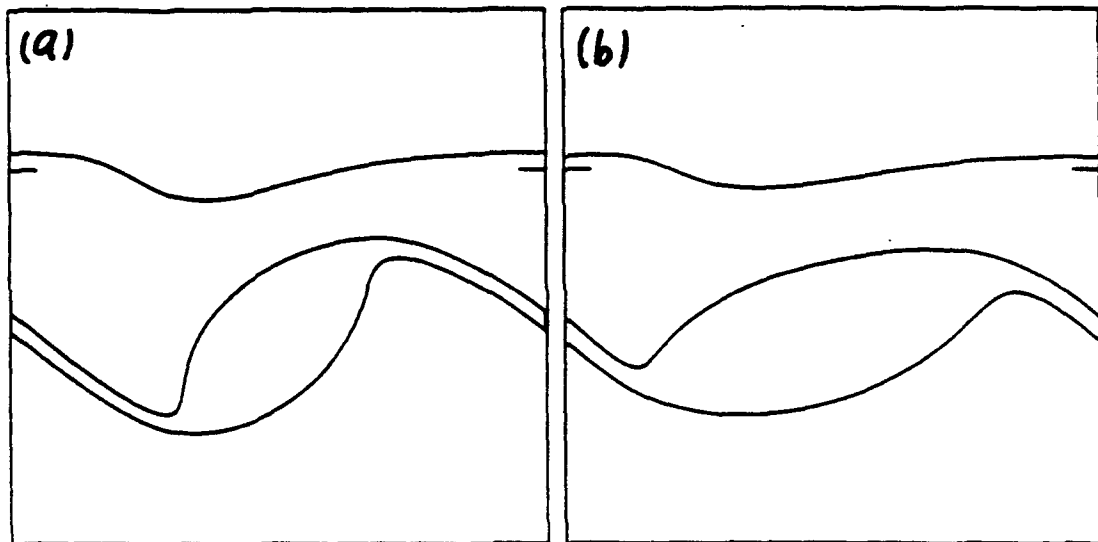


Fig. 8

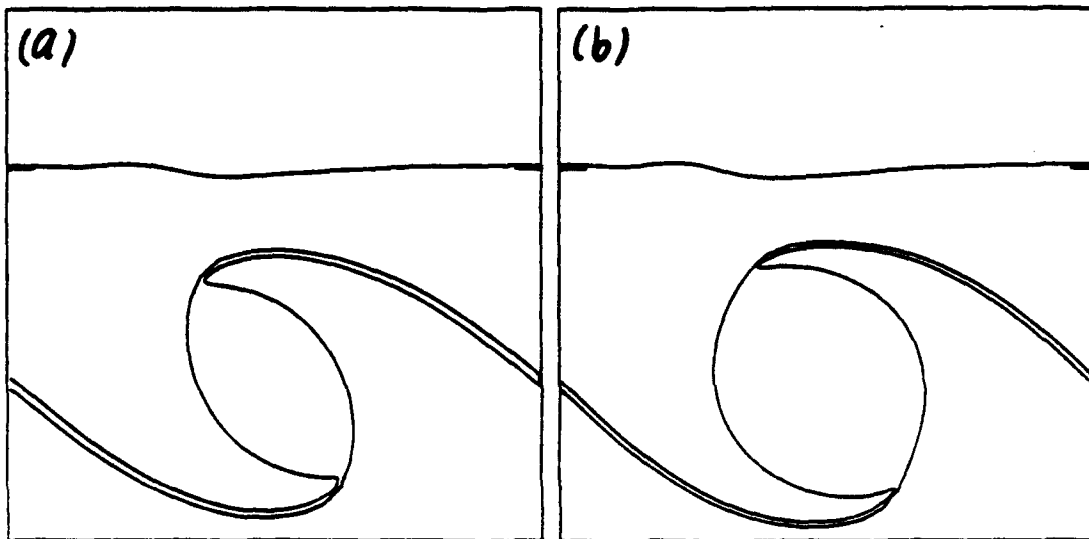


Fig. 9

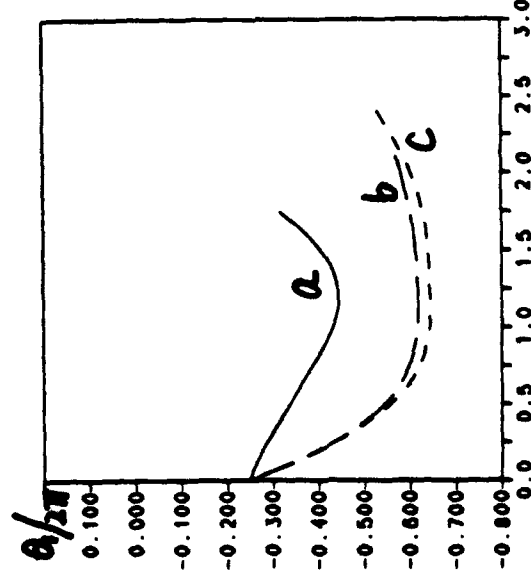
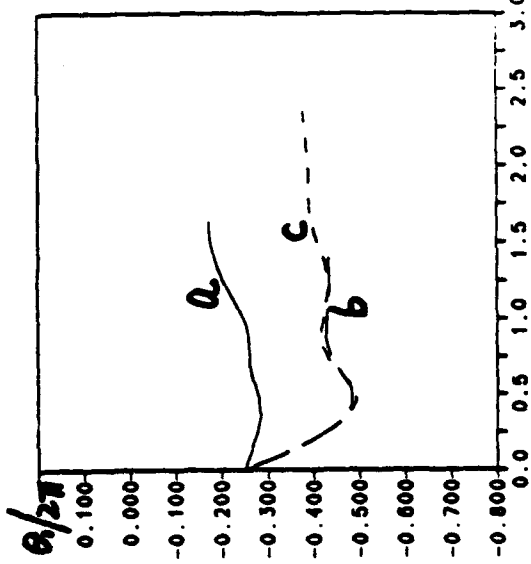
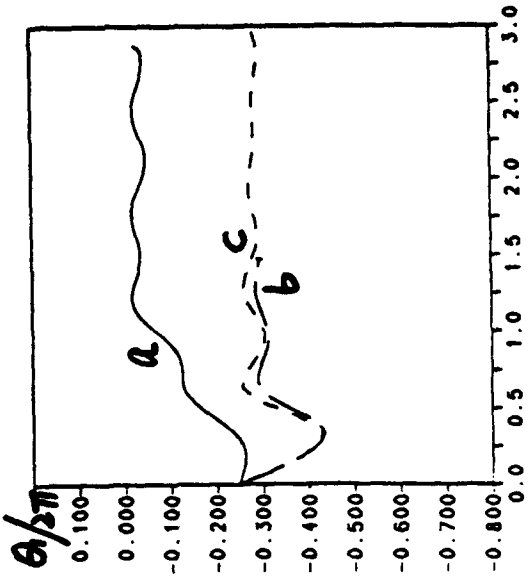
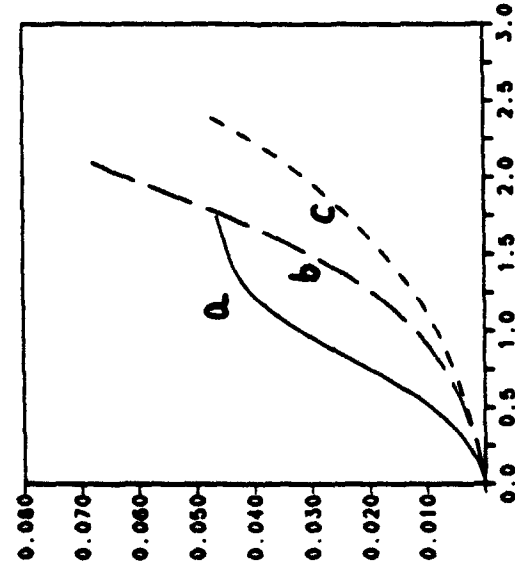
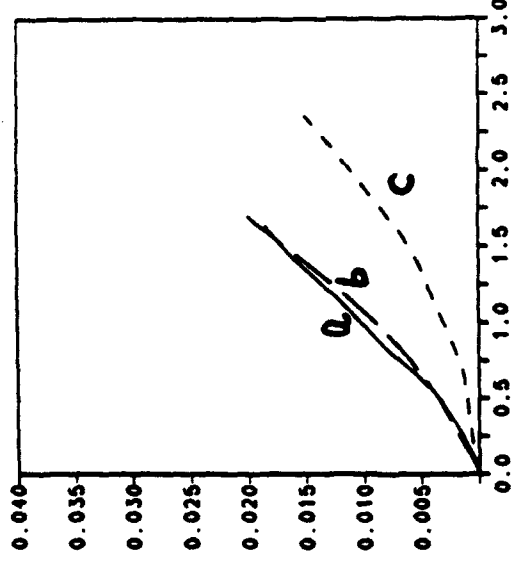
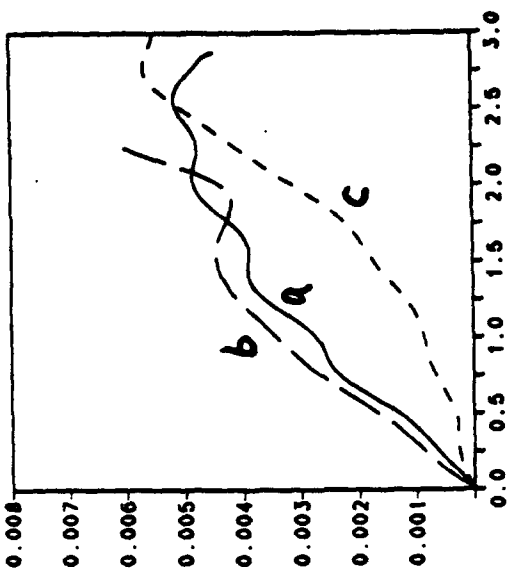


Fig 10

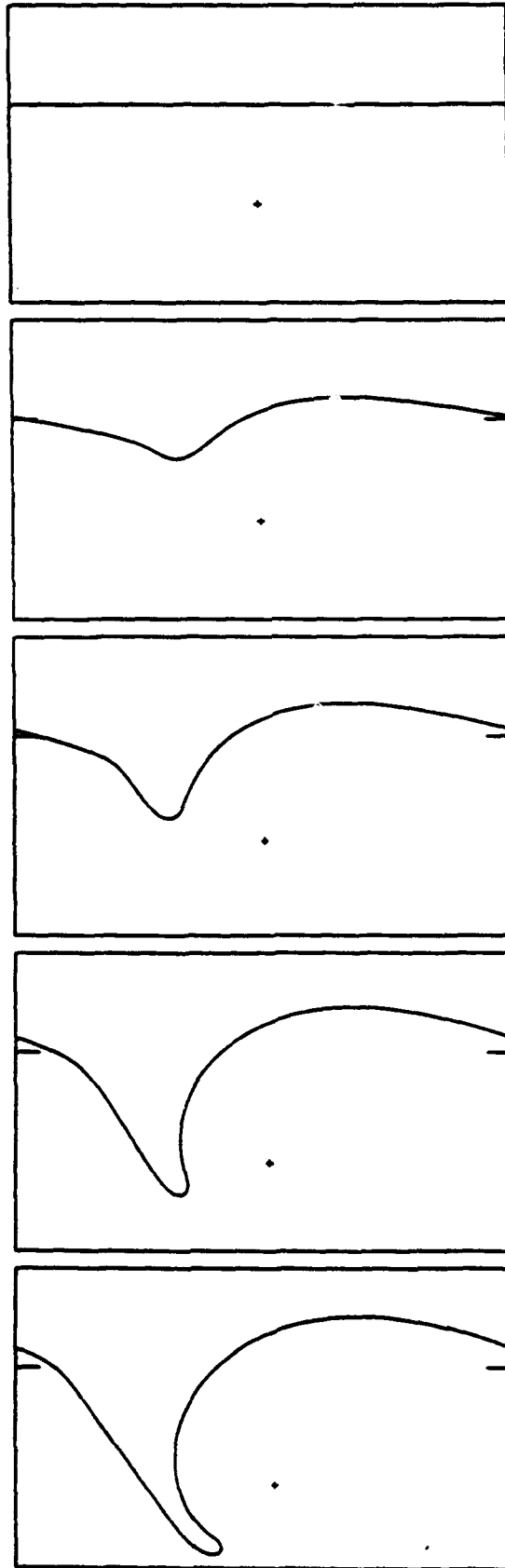


Fig. //

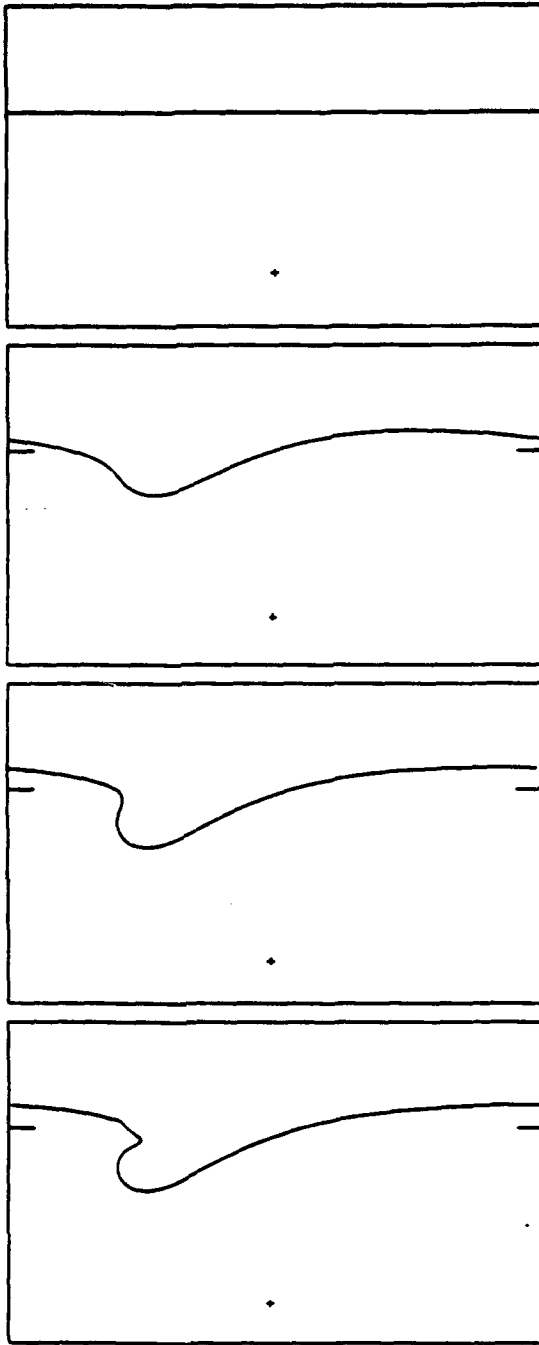


Fig. 12

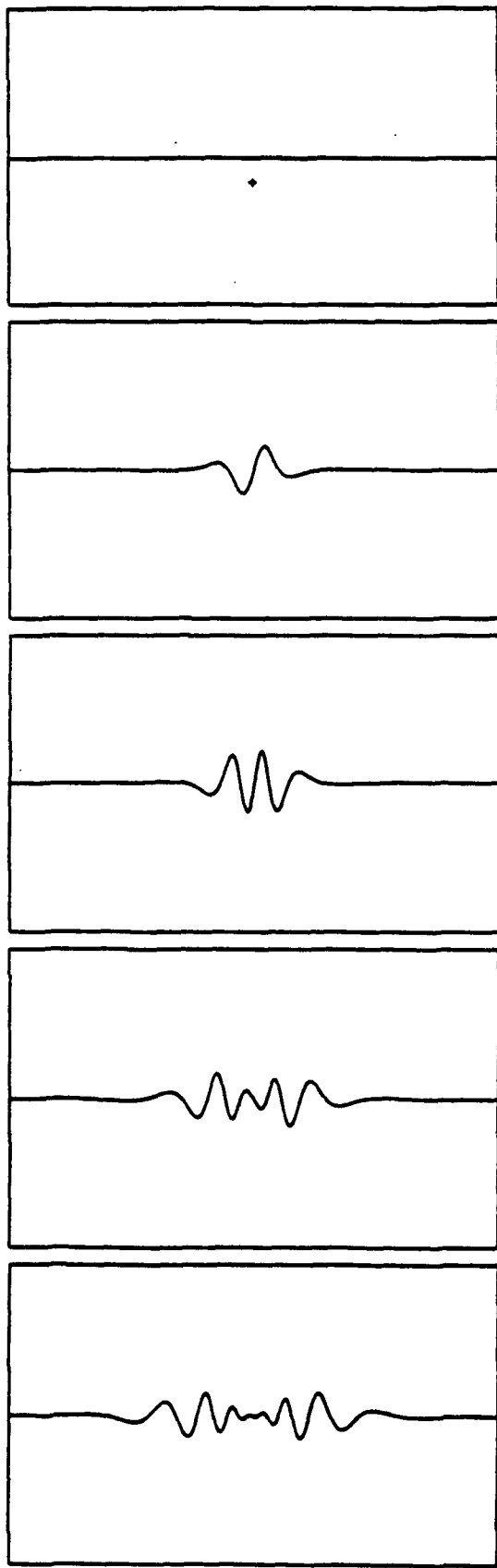


Fig. 13

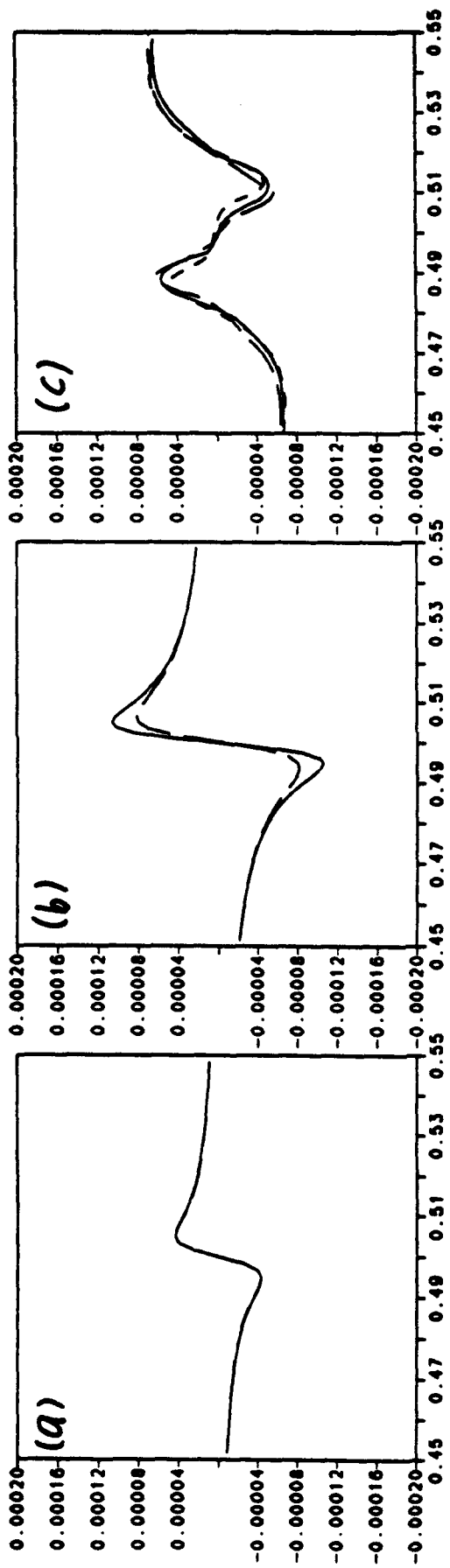


Fig 14

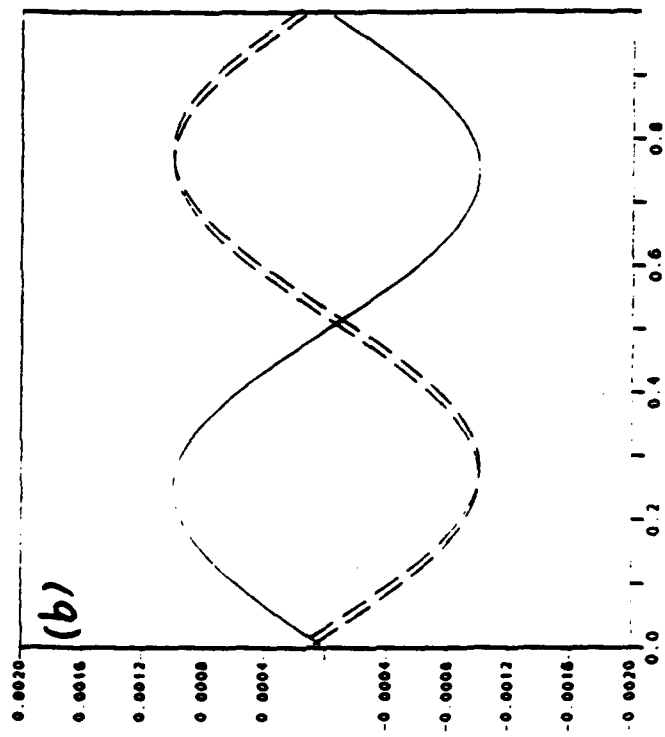
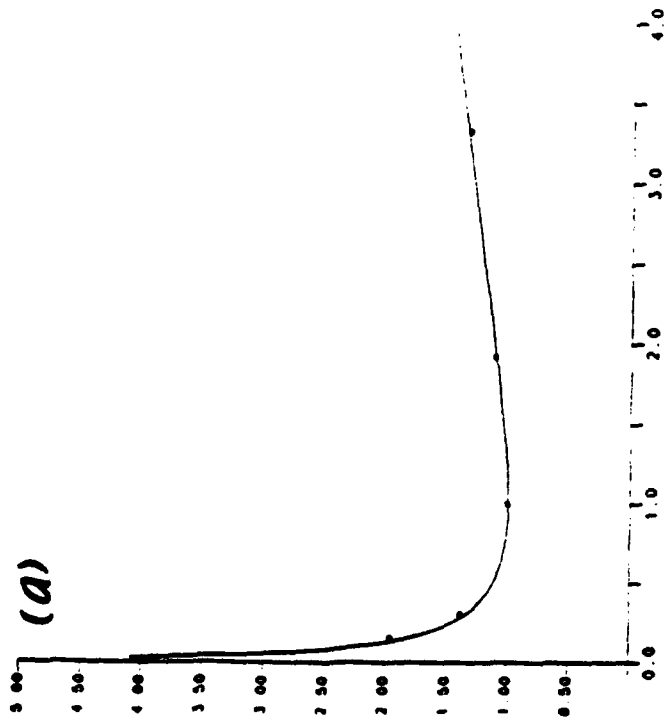


Fig 15

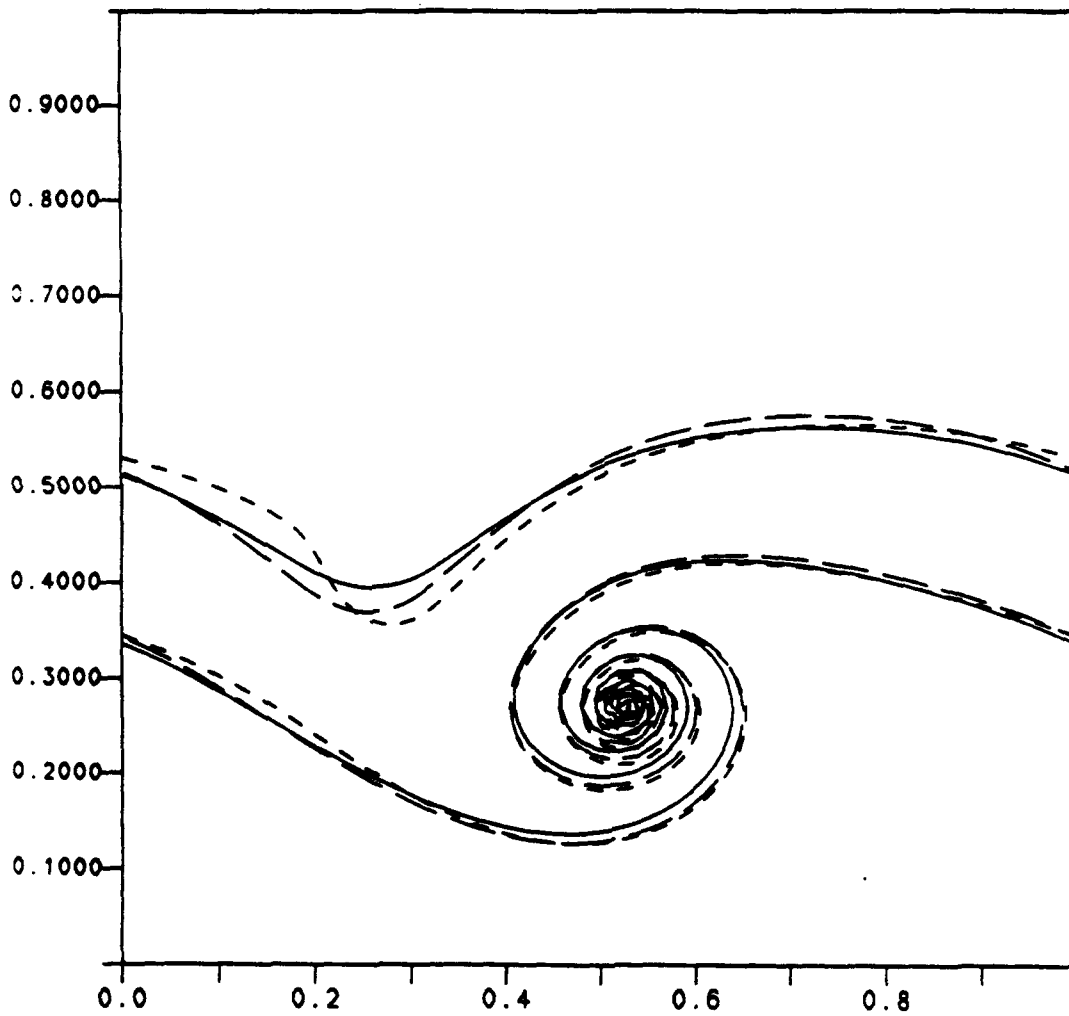


Fig 16

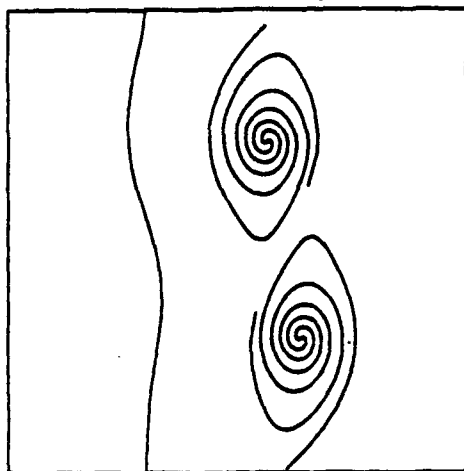
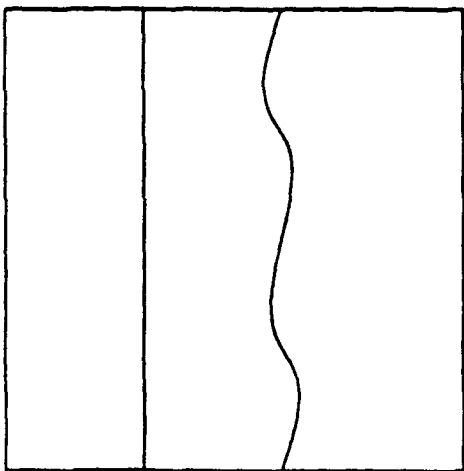
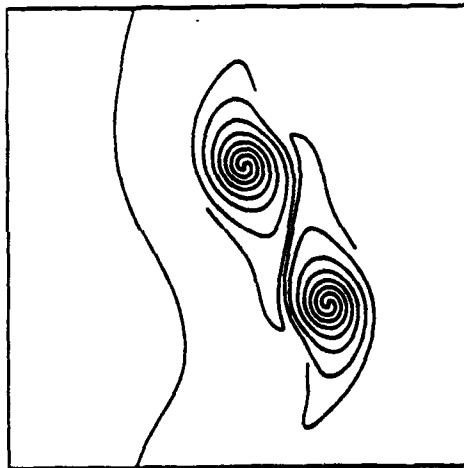
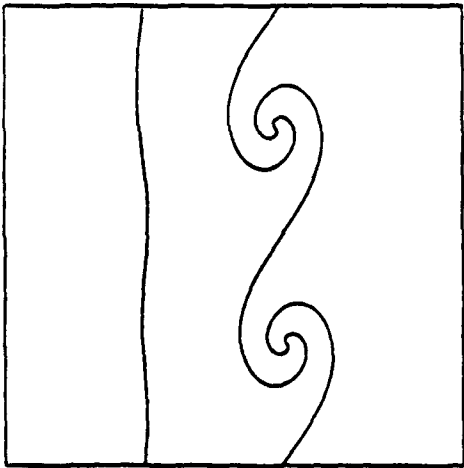
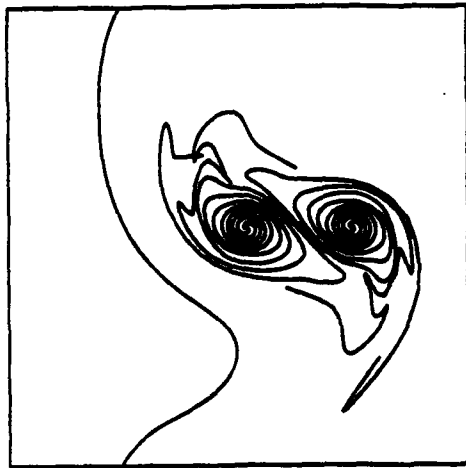
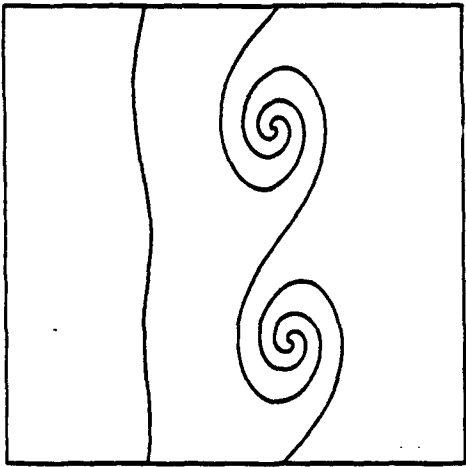


Fig 17

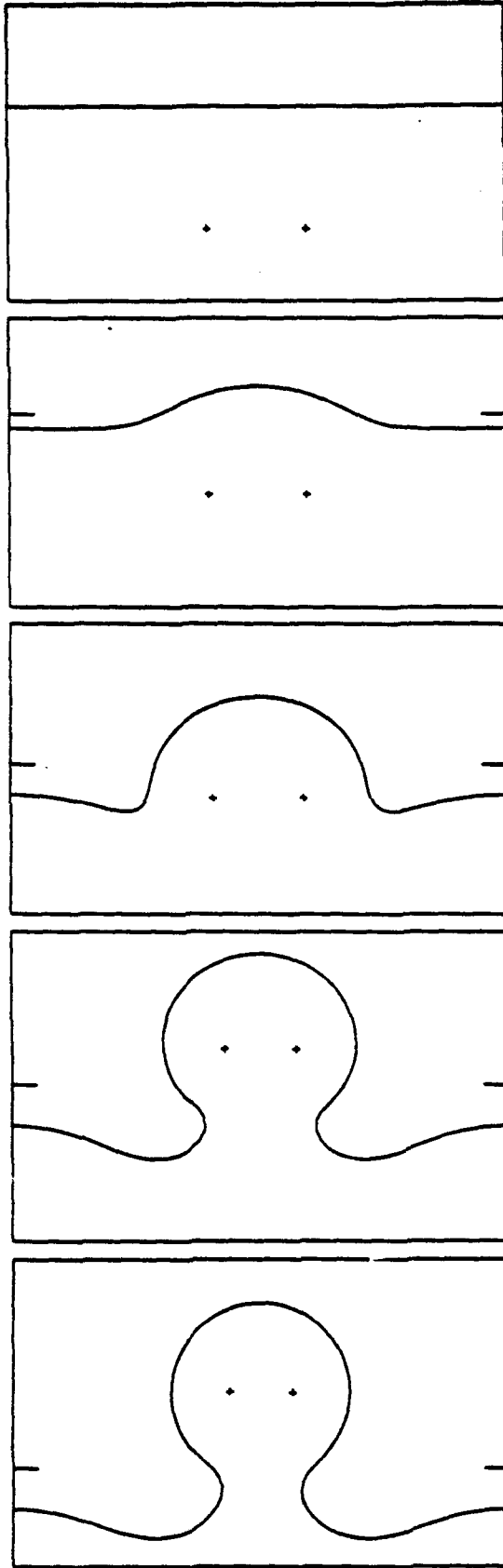


Fig. 18

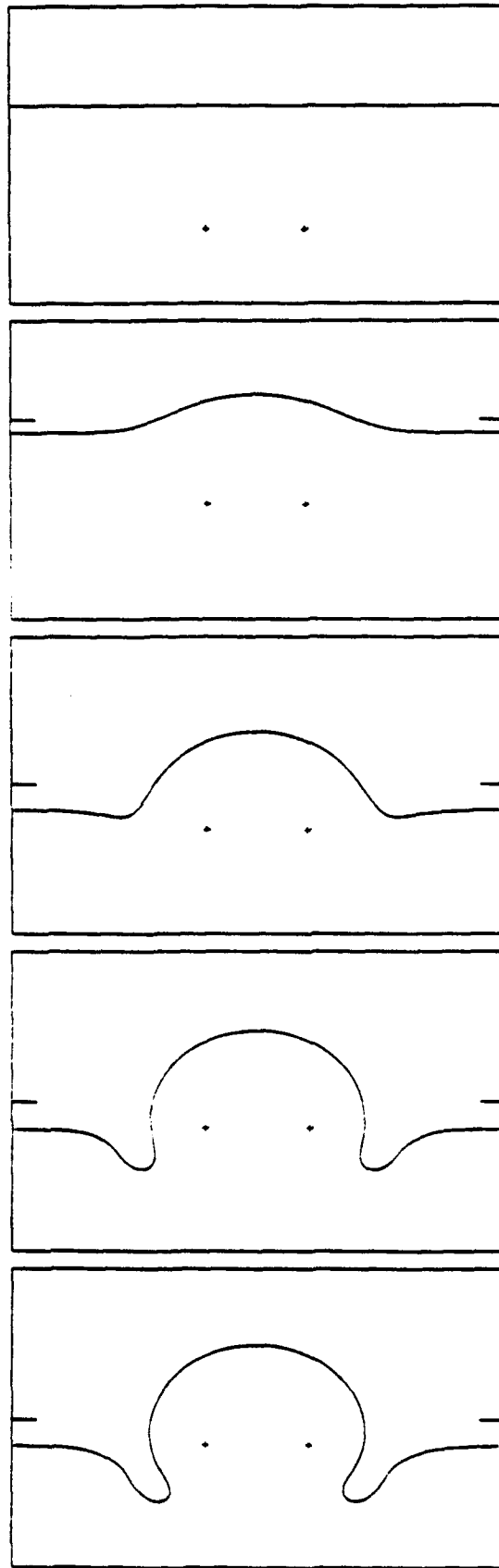


Fig. 19

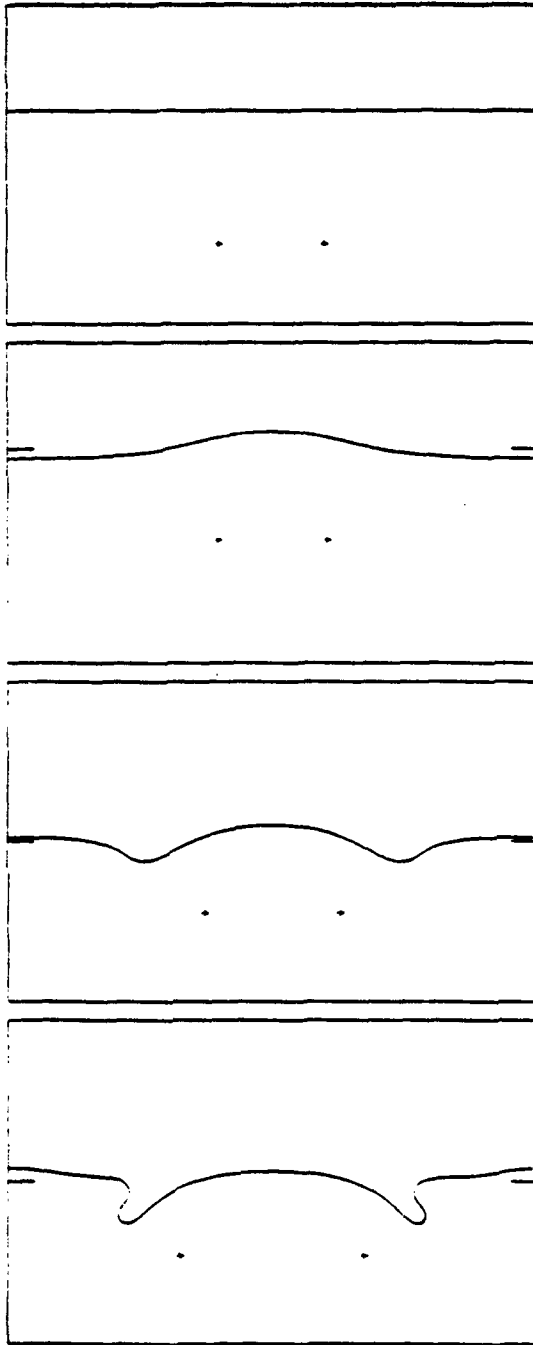
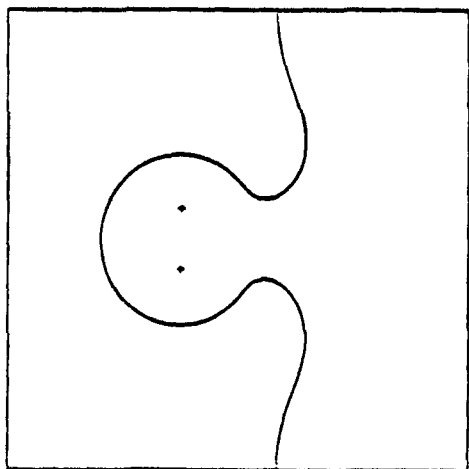
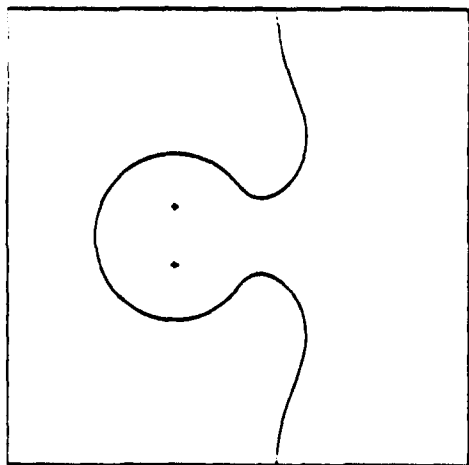
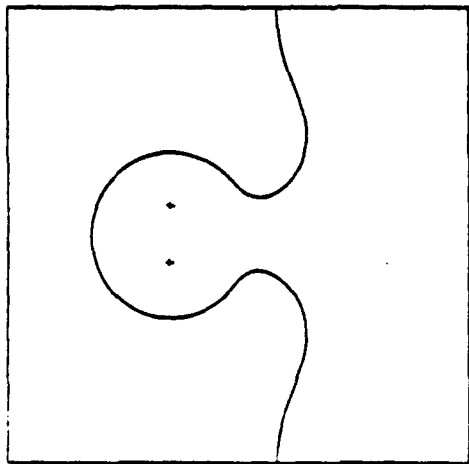


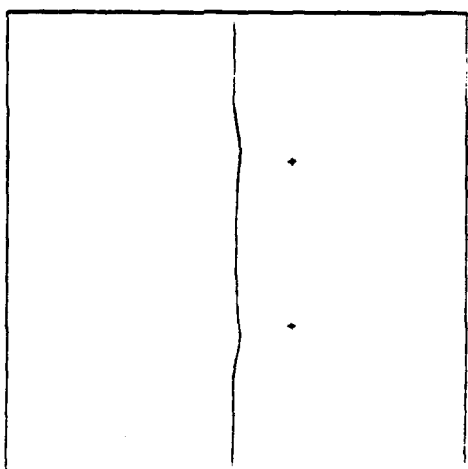
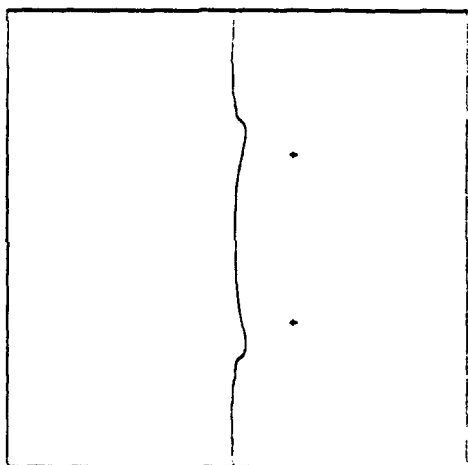
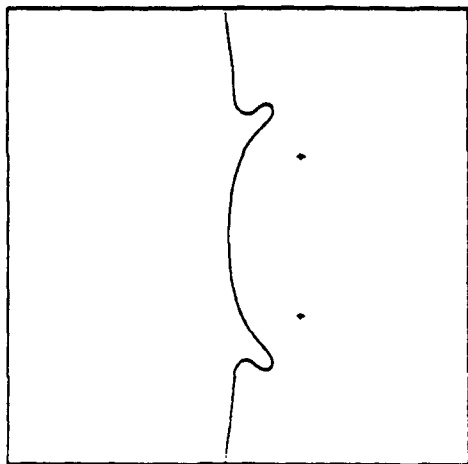
Fig. 20



a

b

c



d

e

f

Fig 21

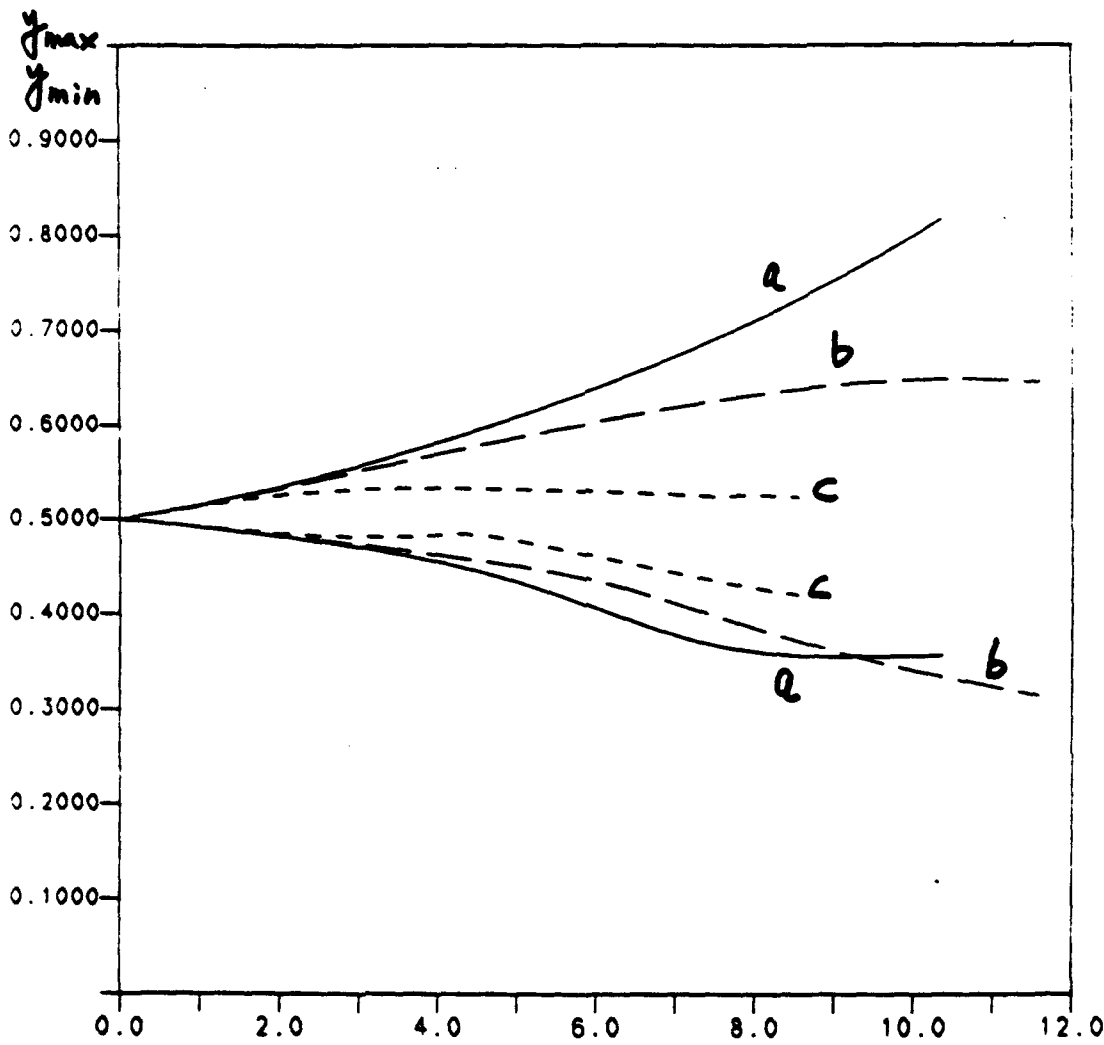


Fig 22a

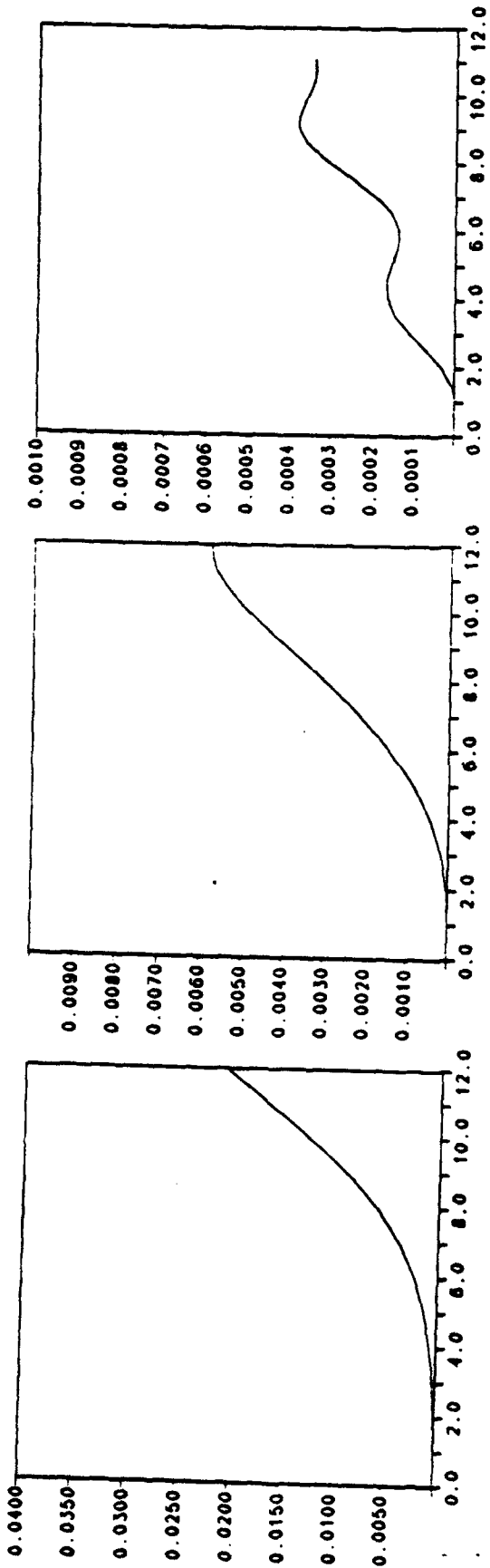


Fig 22b

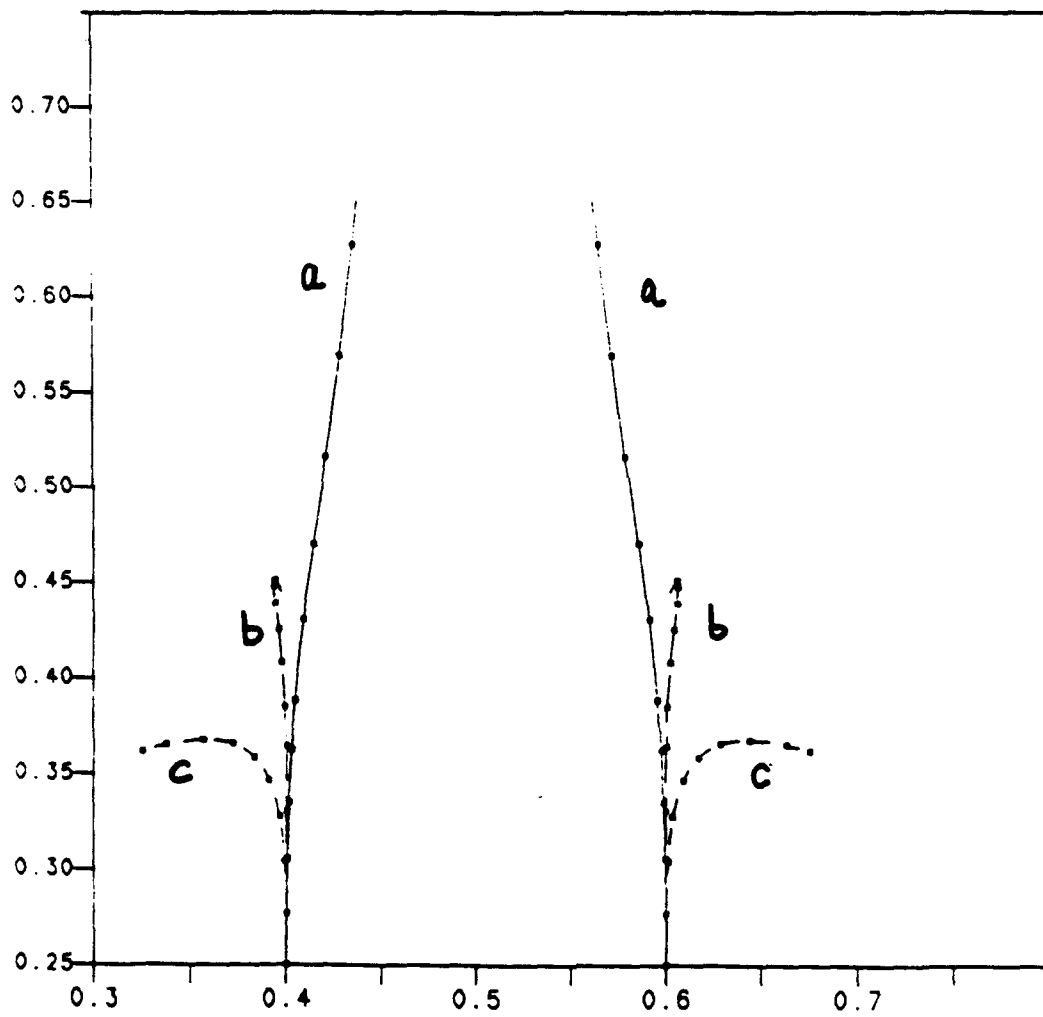


Fig 23

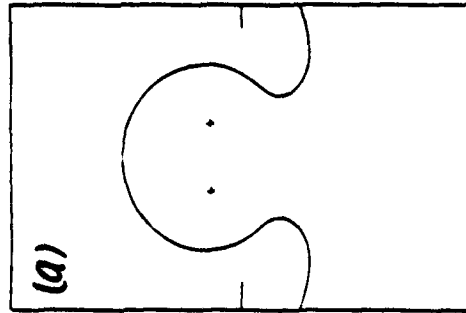
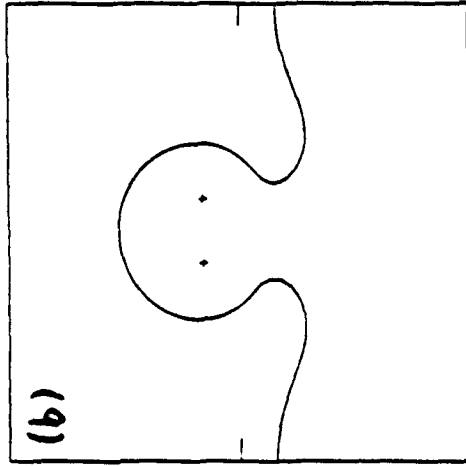
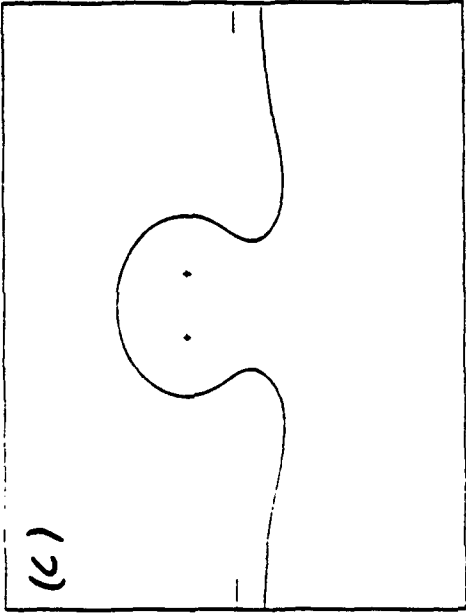


Fig 24

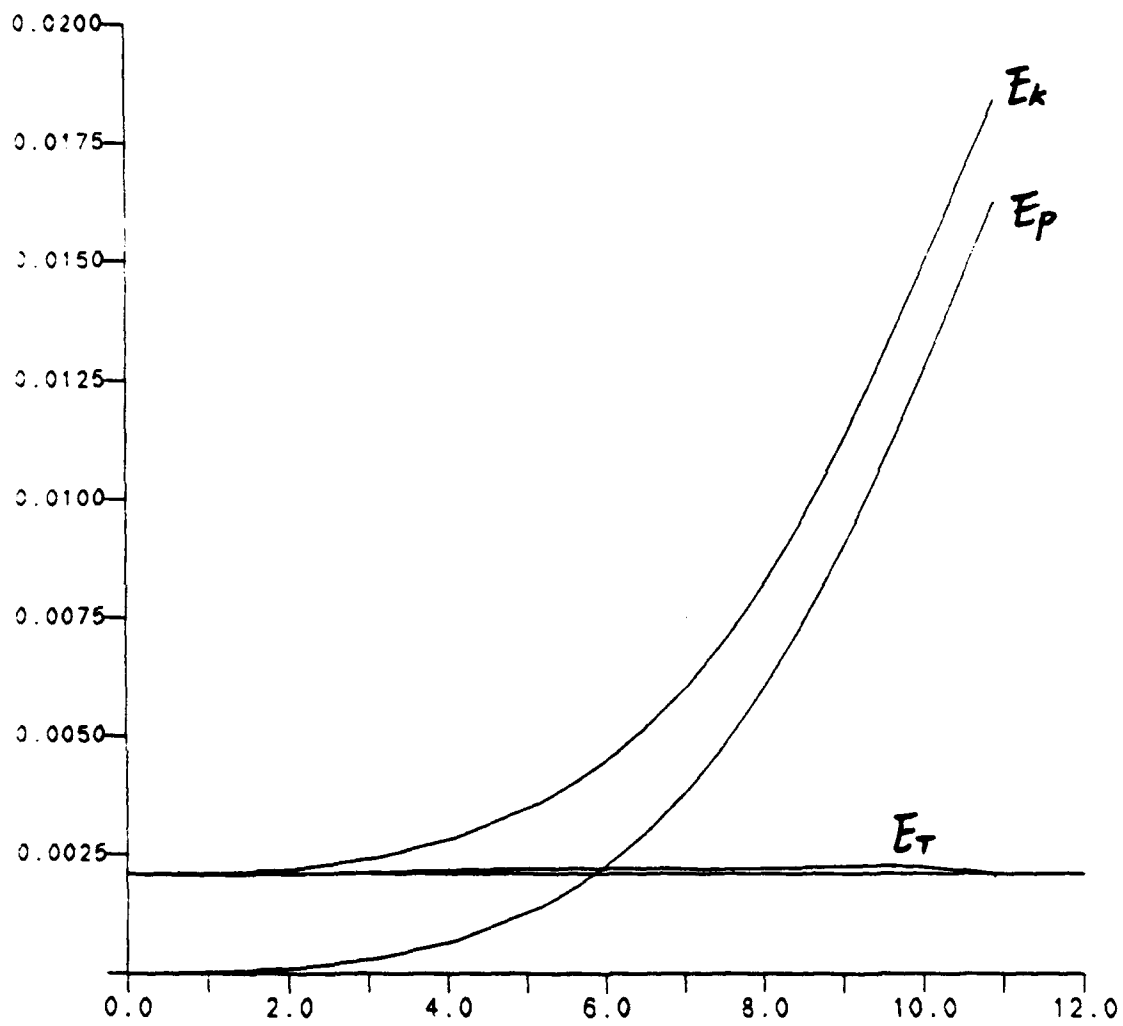


Fig 25

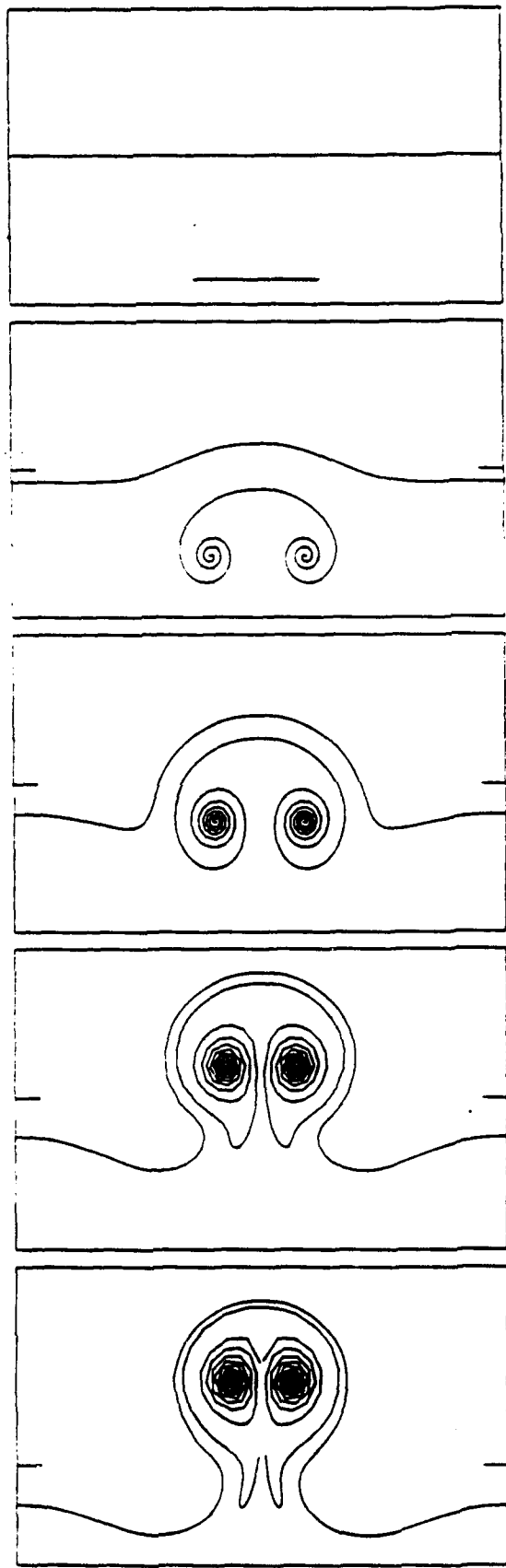


Fig. 26

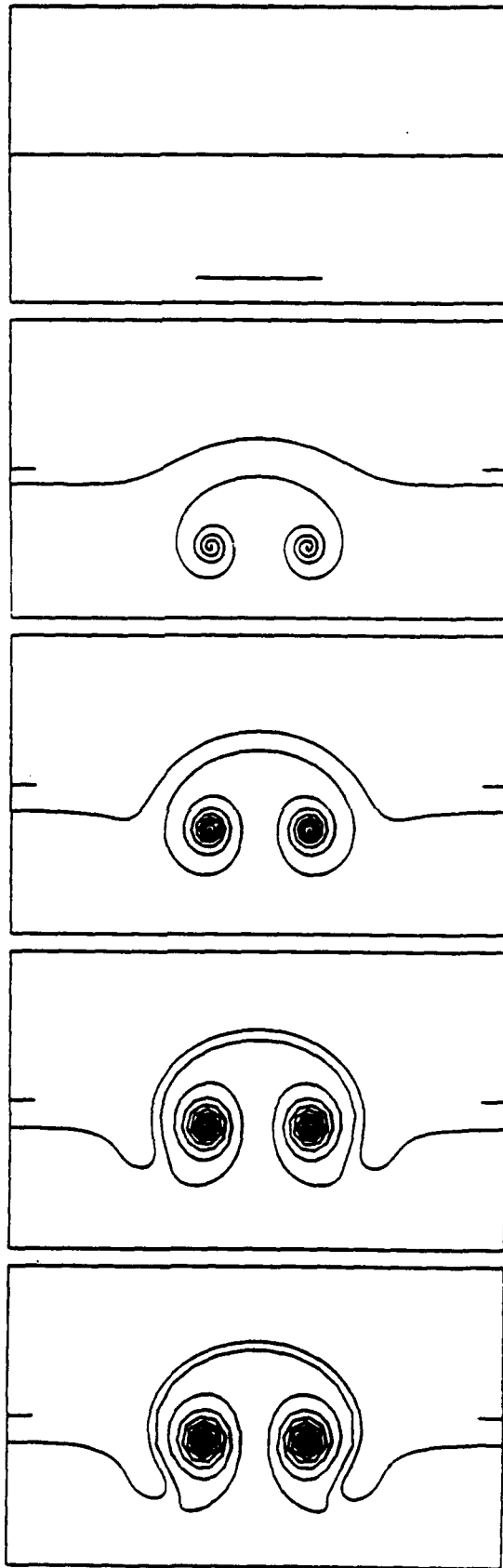


Fig. 27

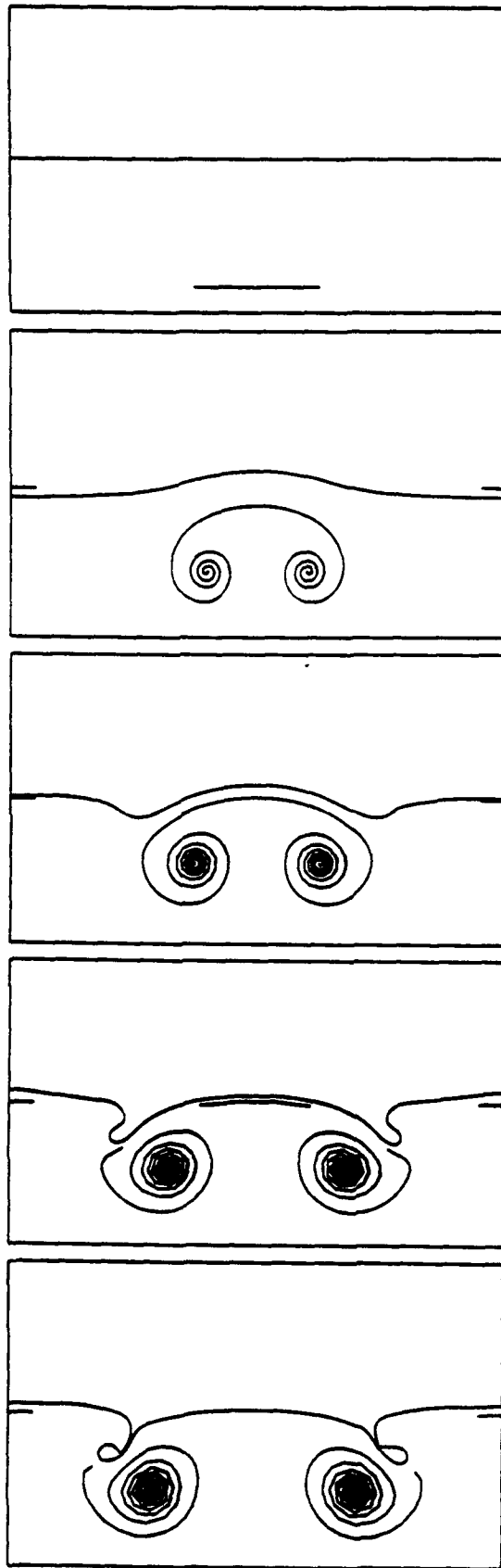


Fig. 28

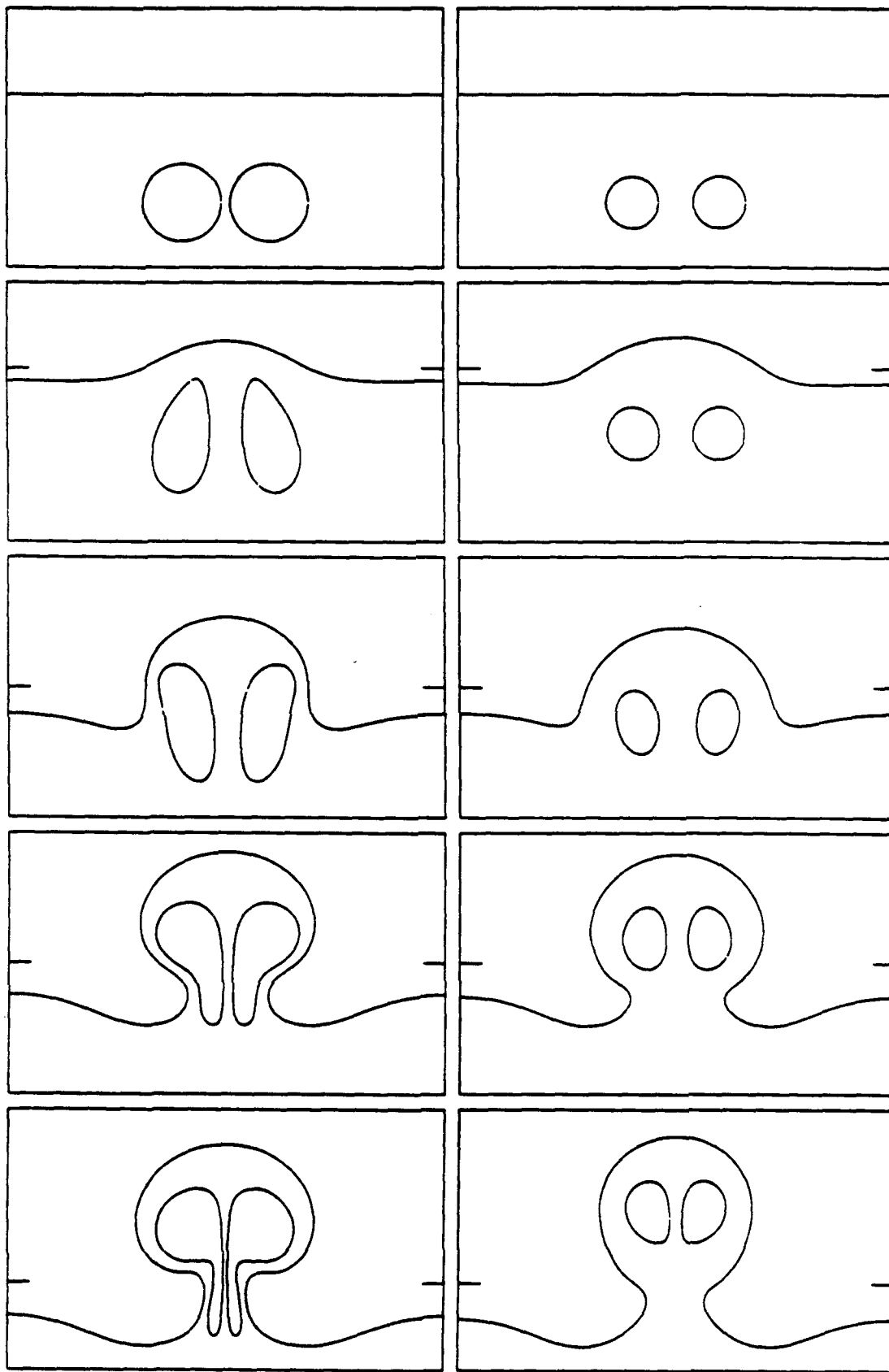


Fig. 29 *a*

b

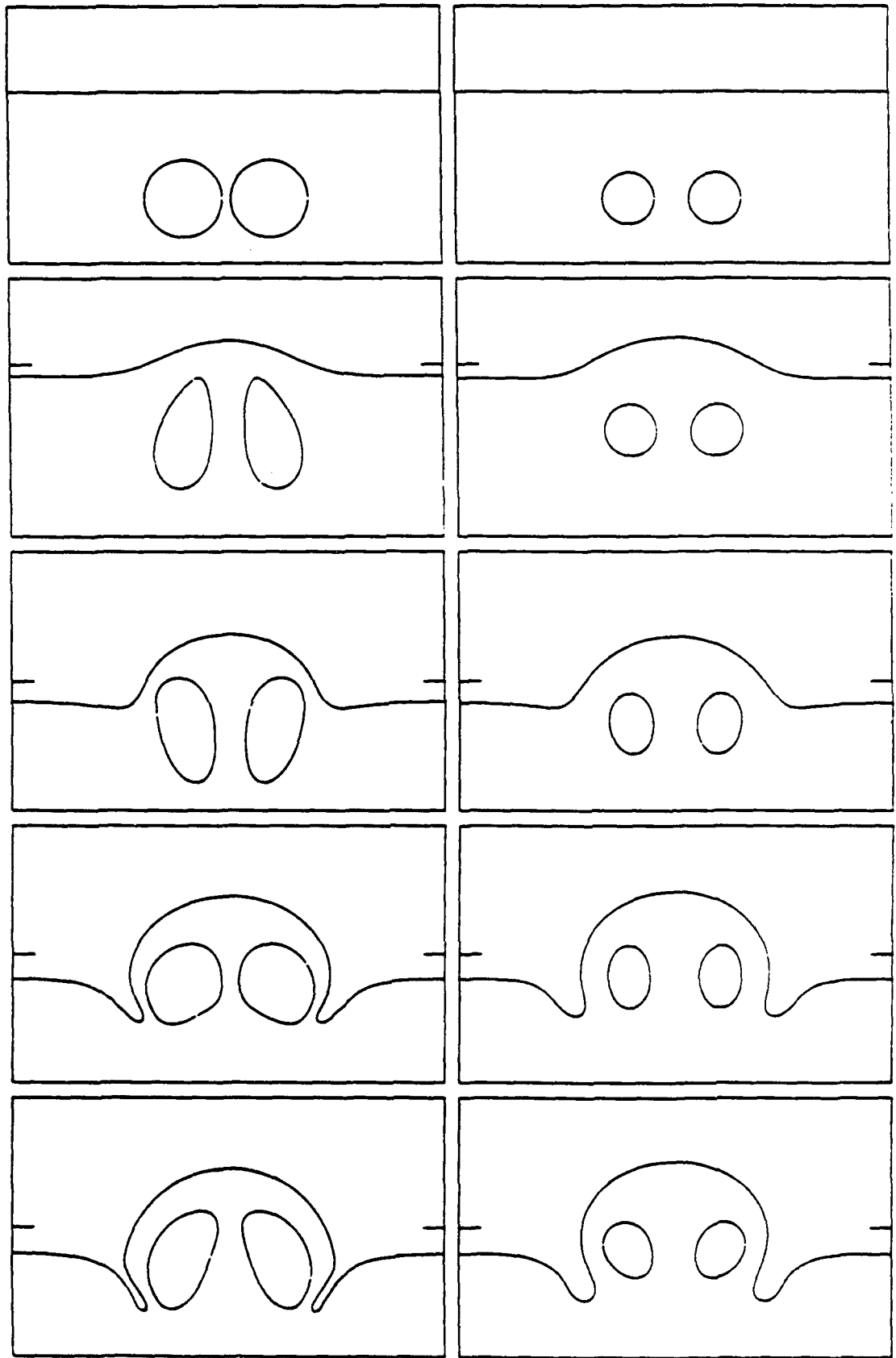


Fig. 30

a

b

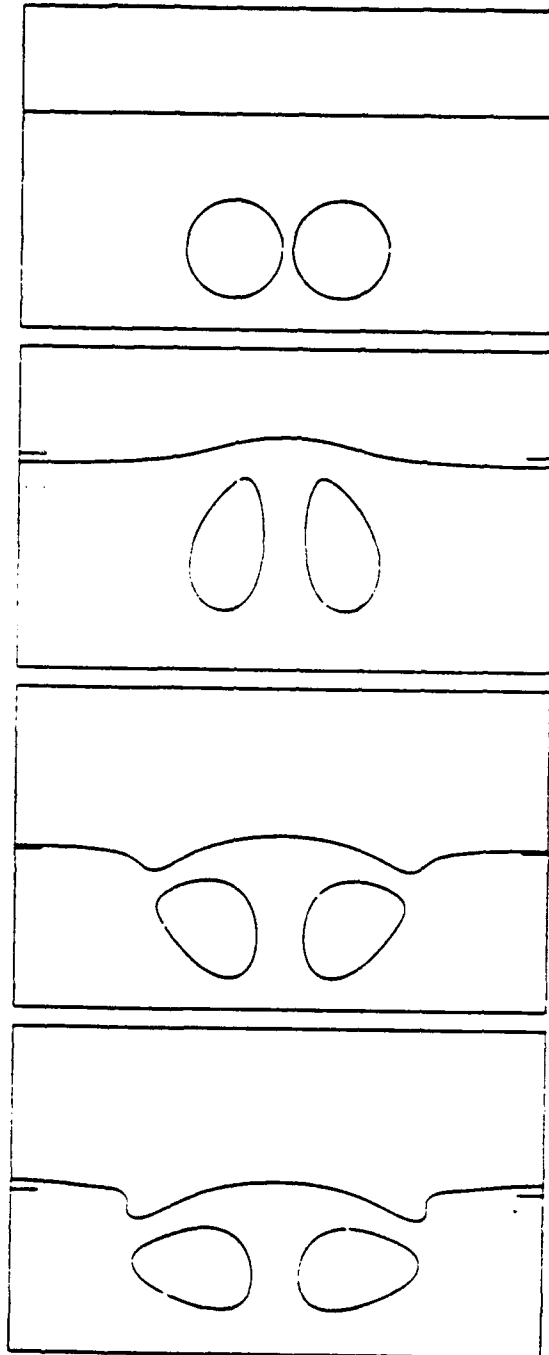
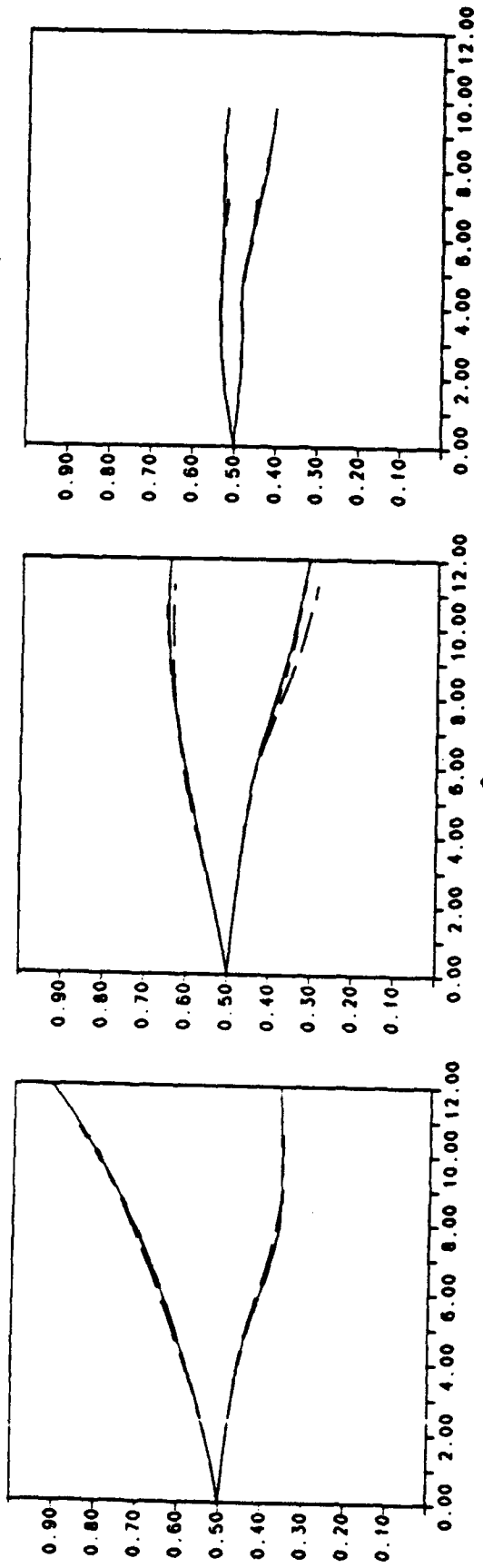
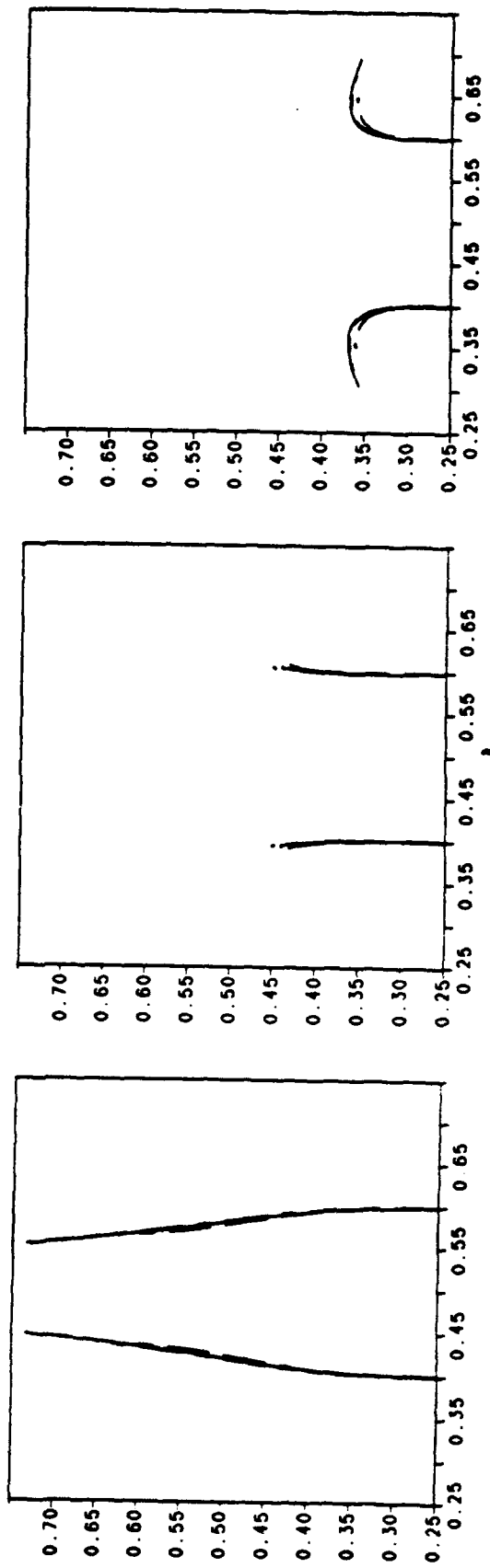


Fig. 31



(a)



(b)

Fig 32

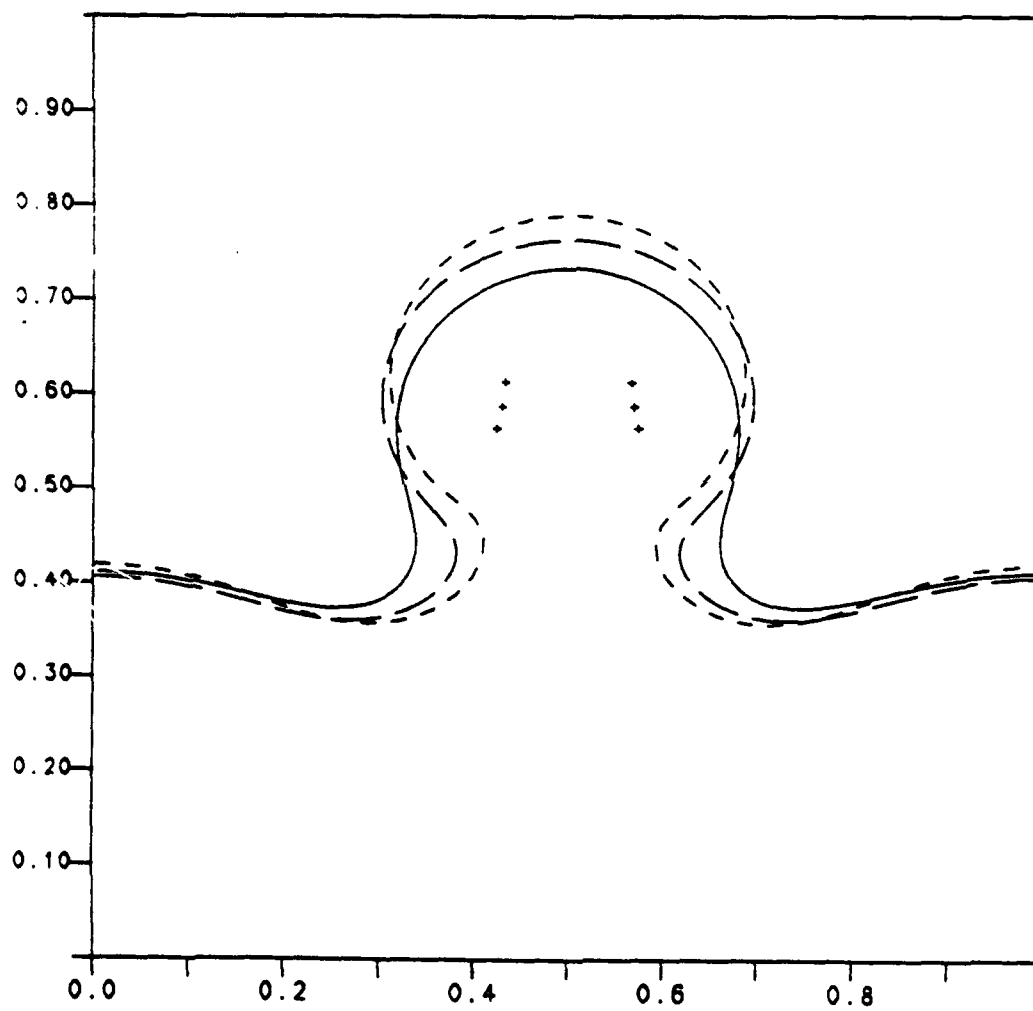


Fig 33

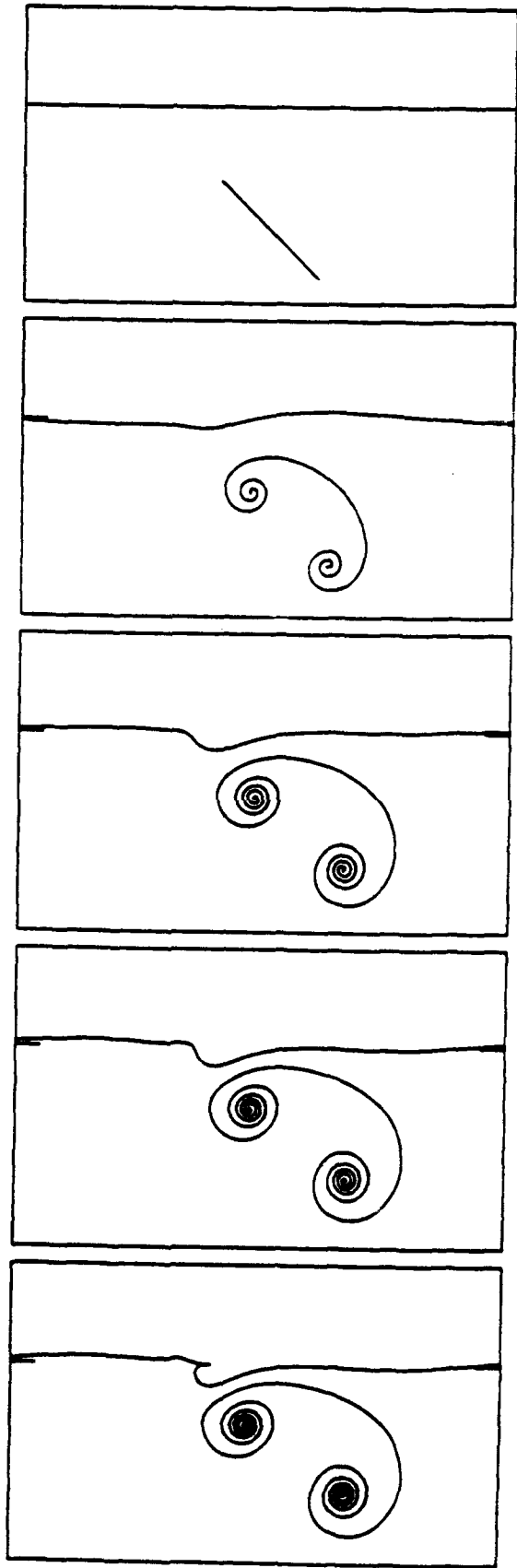


Fig. 34